Stalagmite evidence for Early Holocene multidecadal hydroclimate variability in Ethiopia

Asfawossen Asrat[a,b,*], Andy Baker[c], Wuhui Duan[c,d,e], Melanie J. Leng[f,g], Ian Boomer[h], Rabeya Akter[i], Gregoire Mariethoz[j], Lewis Adler[i], Catherine N. Jex[k], Meklit Yadeta[l], Lisheng Wang[d,m,n]

[a]Department of Mining and Geological Engineering, Botswana International University of Science and Technology, Private Bag 16, Palapye, Botswana
[b]School of Earth Sciences, Addis Ababa University, P. O. Box. 1176, Addis Ababa, Ethiopia
[c]PANGEA Research Centre, School of Biological, Earth and Environmental Sciences, UNSW Sydney, Sydney, NSW, 2052, Australia
[d]Key Laboratory of Cenozoic Geology and Environment, Institute of Geology and Geophysics, Chinese Academy of Sciences, Beijing, China, 100029
[e]CAS Center for Excellence in Life and Paleoenvironment, Beijing, China, 100044
[f]National Environmental Isotope Facility, British Geological Survey, Keyworth, UK
[g]School of Biosciences, University of Nottingham, UK
[h]School of Geography, Earth and Environmental Sciences, University of Birmingham, Edgbaston, Birmingham, UK
[i]Mark Wainwright Analytical Centre, UNSW Sydney, Sydney, 2052, Australia
[j]Institute of Earth Surface Dynamics, University of Lausanne, CH-1015, Switzerland
[k]Geological Survey of Denmark and Greenland (GEUS), Copenhagen, Denmark
[l]Department of Geology, Selale University, P. O. Box 245, Fiche, Ethiopia
[m]University of Chinese Academy of Sciences, Beijing 100049, China
[n]Innovation Academy for Earth Sciences, Chinese Academy of Sciences, Beijing 100029, China

[*]Corresponding author: kassayea@biust.ac.bw (A. Asrat)

Stalagmite evidence for Early Holocene multidecadal hydroclimate variability in Ethiopia

Asfawossen Asrat[a,b,*], Andy Baker[c], Wuhui Duan[c,d,e], Melanie J. Leng[f,g], Ian Boomer[h], Rabeya Akter[i], Gregoire Mariethoz[j], Lewis Adler[i], Catherine N. Jex[k], Meklit Yadeta[l], Lisheng Wang[d,m,n]

[a]Department of Mining and Geological Engineering, Botswana International University of Science and Technology, Private Bag 16, Palapye, Botswana

[b]School of Earth Sciences, Addis Ababa University, P. O. Box. 1176, Addis Ababa, Ethiopia

[c]PANGEA Research Centre, School of Biological, Earth and Environmental Sciences, UNSW Sydney, Sydney, NSW, 2052, Australia

[d]Key Laboratory of Cenozoic Geology and Environment, Institute of Geology and Geophysics, Chinese Academy of Sciences, Beijing, China, 100029

[e]CAS Center for Excellence in Life and Paleoenvironment, Beijing, China, 100044

[f]National Environmental Isotope Facility, British Geological Survey, Keyworth, UK

[g]School of Biosciences, University of Nottingham, UK

[h]School of Geography, Earth and Environmental Sciences, University of Birmingham, Edgbaston, Birmingham, UK

[i]Mark Wainwright Analytical Centre, UNSW Sydney, Sydney, 2052, Australia

[j]Institute of Earth Surface Dynamics, University of Lausanne, CH-1015, Switzerland

[k]Geological Survey of Denmark and Greenland (GEUS), Copenhagen, Denmark

[l]Department of Geology, Selale University, P. O. Box 245, Fiche, Ethiopia

[m]University of Chinese Academy of Sciences, Beijing 100049, China

[n]Innovation Academy for Earth Sciences, Chinese Academy of Sciences, Beijing 100029, China

[*]Corresponding author: kassayea@biust.ac.bw (A. Asrat)

ABSTRACT

A multiproxy oxygen and carbon isotope ($\delta^{13}C$ and $\delta^{18}O$), growth rate and trace element stalagmite paleoenvironmental record is presented for the Early Holocene from Achere Cave, Ethiopia. The annually laminated stalagmite grew from 10.6 to 10.4 ka, and from 9.7 to 9.0 ka with a short hiatus at ~9.25 ka. Using oxygen and carbon isotopic, and cave monitoring data, we demonstrate that the stalagmite deposition is out of isotopic equilibrium, yet trace element and isotope geochemistry is sensitive to hydroclimate variability. Variogram analysis of annual growth rate data suggests that this proxy can only contain hydroclimate information over less than 28-year timescales. Statistically significant and coherent spectral frequencies in $\delta^{13}C$ and $\delta^{18}O$ are observed at 15-25 and 19-23 years respectively. Combined with compelling evidence for deposition out of isotope equilibrium, the observed ~1 ‰ amplitude variability in stalagmite $\delta^{18}O$ is likely forced by non-equilibrium deposition, likely due to kinetic effects during the progressive degassing of CO_2 from the water film during stalagmite formation. These frequencies are similar to the periodicity reported for Holocene stalagmite records from Ethiopian caves, suggesting that multidecadal variability in stalagmite $\delta^{18}O$ is typical. We hypothesise that a hydroclimate forcing, such as runs of one or more years of low annual rainfall, is likely to be the primary control on the extent of the partial evaporation of soil and shallow epikarst water, which is subsequently modulated by karst hydrology, and the extent of in-cave non-equilibrium stalagmite deposition. Combined with possible recharge-

biases in drip water $\delta^{18}O$, modulated by karst hydrology, these processes can generate multidecadal $\delta^{18}O$ variability which can operate with opposite signs. Comparison of Early Holocene $\delta^{18}O$ stalagmite records from the monsoon regions of Ethiopia, Oman and central China show different multi-decadal $\delta^{18}O$ signals, implying regional difference in climate forcing. Seismic activities due to the active tectonics in the region control the frequency of growth gaps (hiatuses) by changing the water flow paths to the stalagmite.

Key Words: Early Holocene, multi-decadal variability, eastern Africa, paleoclimate, Oxygen isotopes

1. Introduction

A number of major air streams and convergence zones influence the modern climate in Ethiopia and the larger Horn of Africa region (Nicholson, 2017). Rainfall amount and intensity in Ethiopia is determined by the annual migration of the African rain belt, which is associated with the movement of the Intertropical Convergence Zone (ITCZ). The annual migration of the ITCZ determines the onset, duration and termination of the East African monsoon, leading to a strongly bimodal annual cycle, resulting in two rainy seasons: the 'big rains' or summer rains (between June and September), which is dependable and whose maxima migrates with the position of the ITCZ, and a second rainy season, the 'small rains' or spring rains, which is less consistent and occurs between March and May with maxima in April.

In addition, East-West adjustments in the zonal Walker circulation regulated by the El Niño-Southern Oscillation (ENSO) and the Indian Ocean Dipole (IOD) cause short-term (annual to decadal) fluctuations in the intensity of precipitation in Ethiopia. These are possibly a direct response to sea-surface temperature (SST) variations in the Indian and Atlantic Oceans, which are in turn affected by the ENSO and the IOD (Nicholson, 2017; Taye et al., 2021). While the global-scale atmospheric circulation patterns determine the rainy seasons in Ethiopia, local rainfall distribution is modulated by the topographic features such as the highland barriers separated by a rift zone (Asrat et al., 2018).

Nearly 80 % of the >100 million people inhabiting Ethiopia depend on rain-fed agriculture for their subsistence. Both the summer and spring rains in most parts of the country are important for adequate and sustained harvest. However, the interannual variability of the spring rains is higher than the summer rains (e.g., Viste et al., 2013) and failure of the spring rains is common (Diro et al., 2008). Failure of the spring crop usually leads to a reduced annual productivity (McCann, 1990) and in most cases leads to famine, at least in some worst-hit parts of the country, such as in 1984 and 2009, the two driest years since 1971 (Viste et al., 2013). The southeastern Ethiopian lowlands were affected by failure of the spring rains as recently as the 2013/2014 and 2015/2016 growing seasons.

There has been a general decline in the reliability of the spring rains since 1979 (e.g., Williams and Funk 2011; Viste et al., 2013), and data on the failure of the spring rains for the modern era suggests this occurs at a multidecadal frequency. For instance, within the 1995-2010 period, Viste et al. (2013) identified a cluster of dry spring seasons nationwide in 1999-2004 (except 2001), and in 2008-2011. The causes for the failure of the spring rains remain unclear. However, some studies (e.g., Segele et al., 2009; Williams and Funk, 2011; Viste et al., 2013) agreed that the failure is usually associated with deflections of the transport of moisture to Ethiopia due to atmospheric circulation anomalies. For instance, the 2009 spring drought was largely attributed to the deflection of the easterly flow bringing moisture from the Northern Indian Ocean and the southeasterly flow bringing moisture from the southern and equatorial Indian Ocean, by southwesterly anomalies (Viste et al., 2013).

Paleoclimate records provide a useful insight into the processes determining rainfall climate variability (Bar-Matthews et al., 1997; Hu et al., 2008), such as the multidecadal frequency of failure of the spring rains described earlier. For Ethiopia, annually-laminated records such as those widely present in stalagmites from the country have the necessary temporal resolution to investigate past multi-decadal climate variability (Asrat et al., 2007; 2018; Baker et al., 2007; 2010). Previous research has shown that the strong seasonality of rainfall leads to the ubiquitous formation of annual growth laminae (Asrat et al., 2008). The warm climate leads to a fast stalagmite annual growth rate (100 to 500 µm/yr), permitting high-resolution geochemical analyses. Tectonic activity associated with the adjoining East African Rift System to the cave sites leads to discontinuous stalagmite deposition rarely lasting more than 1,000 years, with stalagmites often having distinctive cone-shaped morphologies indicative of a drainage of a water source (Asrat, 2012). Two discontinuously forming, Early to Middle Holocene stalagmite records from the Mechara caves (Ach-1 and Bero-1 stalagmites) have previously exhibited multidecadal variability in $\delta^{13}C$ and $\delta^{18}O$, as well as growth rate (Asrat et al., 2007; Baker et al., 2010). However, multi-decadal variability in speleothems can be climatically forced, can derive from the inherent non-linear properties of karst hydrology, or can arise from a combination of the two; e.g. non-linear karst processes amplifying the signal from extreme climate events (Baker et al., 2012).

Multi-stalagmite and multi-proxy analyses is essential for investigating the reproducibility of paleoclimate records in speleothems (Hellstrom and McCulloch, 2000; Dorale and Liu, 2003). Here, we present a third high-resolution stalagmite paleoclimate record for the Holocene from Achere Cave, southeastern Ethiopia. Stalagmite Ach-3, which formed in the Early Holocene, is dated by U-Th series and annual laminae, and analysed for $\delta^{13}C$ and $\delta^{18}O$ and trace elements. Combined with geostatistical analyses, we investigate the multidecadal geochemical proxy signal in the stalagmite and compare this to other Middle and Late Holocene stalagmite records from the region.

2. Methods

2.1.Site Description

The Achere cave forms part of the bigger Achere-Aynage cave system and has been previously described (Asrat et al., 2007; 2008). The Achere-Aynage cave system developed along numerous NE-SW oriented parallel rifts on the Southeastern Ethiopian highlands, close to the Main Ethiopian Rift (MER), indicating their development and modification through time in close association with rift forming processes (Fig. 1). The maze-like cave network developed within a narrow, 20-25 m vertical zone, parallel to the bedding of Jurassic limestone. A laterally extensive calcareous mudstone/marl horizon within the limestone currently marks the roof of the cave chambers (Brown et al., 1998; Gunn and Brown, 1998; Asrat et al., 2007; 2008).

The limestone terrain in the Mechara area including the top of the limestone beds forming the Achere-Aynage caves are overlain by very shallow (generally less than 50 cm deep) soils composed of lime-rich, soft calcareous layers overlain by dark organic rich humus layers, classified as rendzinas (Bruggeman, 1986). In the wider area, chromic cambisols develop over the sandstones and shales, which form low hills above the limestone sequence. These soils are in most parts strongly eroded (Asrat et al., 2008).

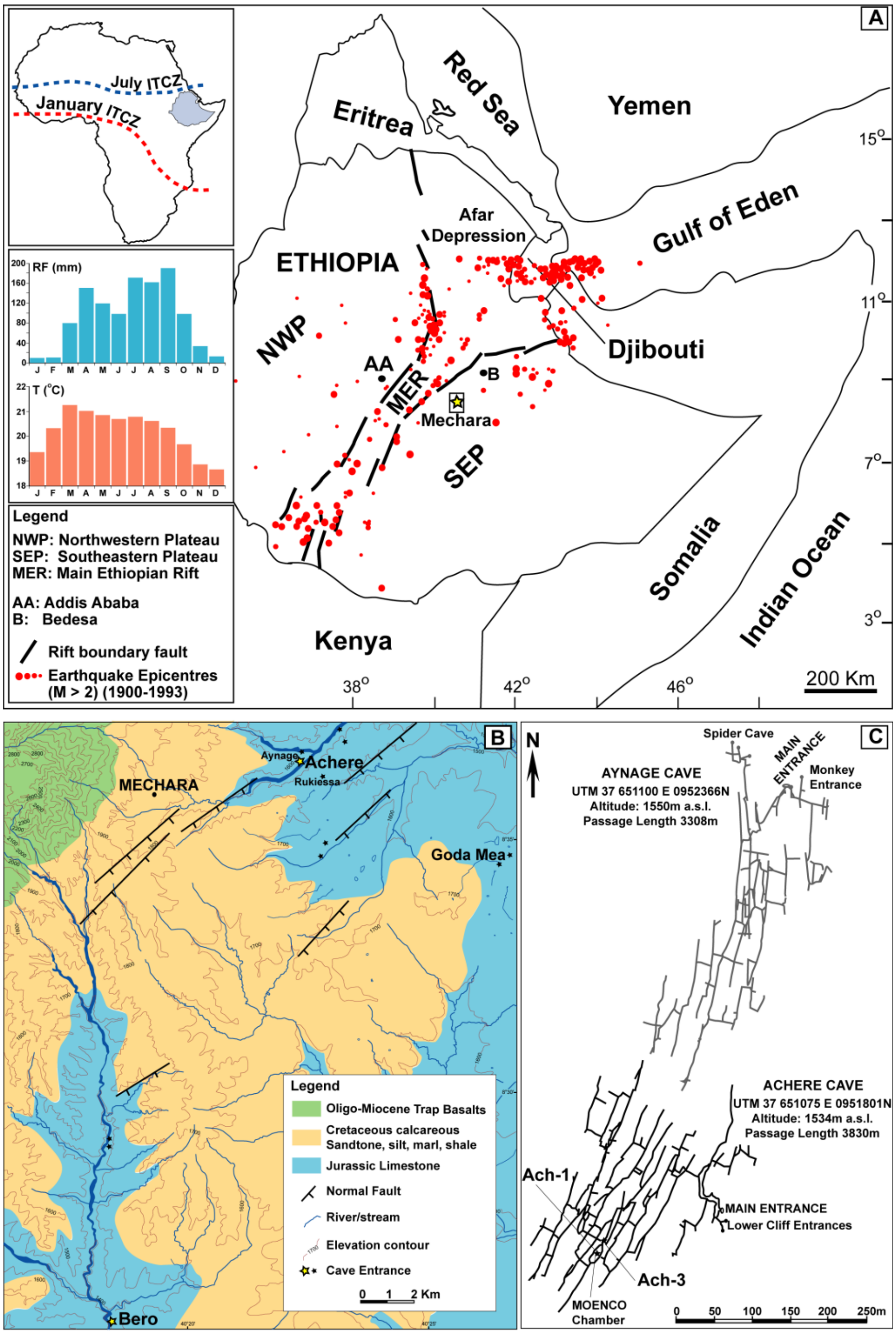

Figure 1. (A) Regional structural setting of Ethiopia showing the location of the Mechara caves. The epicentres of the major earthquakes in the Main Ethiopian Rift and the adjoining highlands are marked (Note that earthquake epicentres in the northern Afar depression are not represented). Insets show the mean position of the ITCZ in July (summer) and January (winter) over Africa; and the mean monthly rainfall (mm) and mean monthly temperature of the Mechara region, at the Bedesa Meteorological Station (1994-2014 data from the Ethiopian Meteorological Agency). Location of Fig. 1(B) is marked by a solid rectangle around the location of Mechara; (B) The topography, geology, structure and drainage system of the Mechara karst area and locations of the entrances to the caves (including Aynage-Achere and Bero); (C) Achere-Aynage cave survey showing the location of stalagmite Ach-3 and a previously published stalagmite, Ach-1. Figures (A) and (B) modified from Asrat et al. (2008; 2018); Fig. (C) modified from Brown et al. (1998).

Asrat et al. (2008) reported cave monitoring data, which indicated that the Ach-3 stalagmite grew in a cave where modern relative humidity is 87.5±11.5 %, within cave pCO_2 content is 745±365 ppm, and has nearly constant within-cave temperature of ~20.5 °C. Drip waters in the cave have Ca^{2+} and Mg^{2+} concentrations of 3.13±1.88 mmol/L and 0.66±0.57 mmol/L, respectively. Compared to the range of drip water Ca^{2+} concentration (= 2.63 ± 2.36 mmol/L) in all the monitored caves in Mechara, the Achere cave drip waters have distinctly higher Ca^{2+} concentration implying "open system" evolution (Baker et al., 2016), where the calcareous (limestone, marl and carbonate rich mudstone) aquifer readily contributes Ca^{2+} ions to the drip waters, and likely lead to rapid calcite formation which could be out of isotope equilibrium. Limited cave drip water oxygen isotope data from Achere cave demonstrate a limited range of $\delta^{18}O$ composition from -1.6 to -0.5 ‰ (n=10) (Asrat et al 2008).

2.2. Sample description

The Achere-Aynage cave system contains abundant speleothems. Ach-3 stalagmite was sampled in Achere cave in April 2004 from a narrow chamber leading to the bigger *Moenco* Chamber (where Ach-1 was sampled, Asrat et al., 2007), about 200 m from the cave entrance. Ach-3 developed on a low, narrow ledge 2 m beneath a roof marked by a mudstone layer. The chamber was dry and the speleothem was inactive at the time of sampling, though some soda straw stalactites in the vicinity of the chamber indicate recent seasonal dripping. Ach-3 is a 420 mm long, slender stalagmite, narrowing from the bottom (120 mm diameter) to the top (60 mm diameter; Fig. 2). The stalagmite was sectioned into two halves, and one half was polished and scanned at high resolution, on which lamina counting in triplicate has been conducted using Image analysis software. Continuous laminae were visible

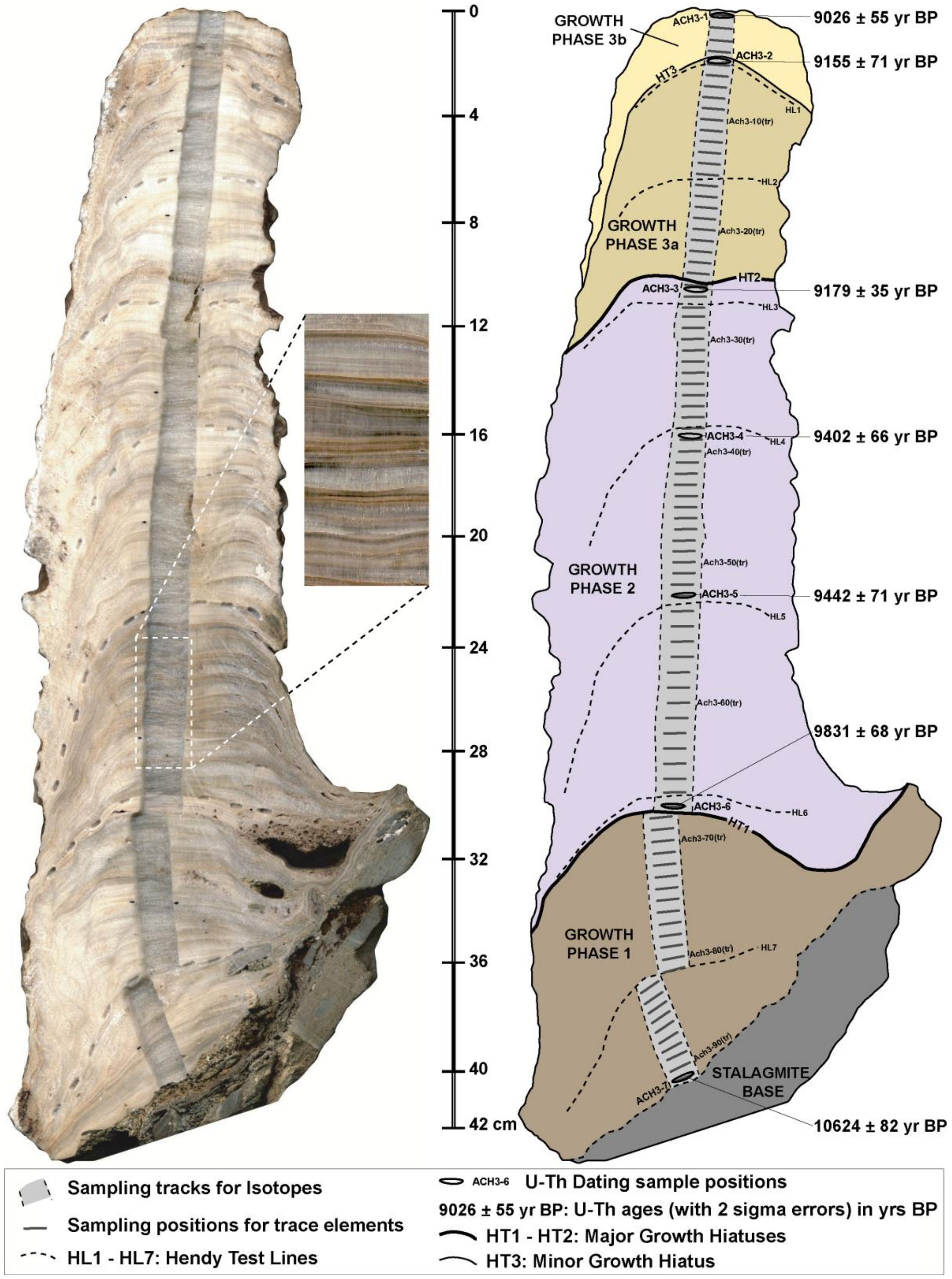

Figure 2. Ach-3 hand-section in both scanned image (left) and sketch (right), showing the four growth phases, locations of the major and minor growth hiatuses, and sampling for isotopes, trace elements and U-Th analyses, and U-Th ages. The central panel is a sample of a high-resolution scan (not to scale) along the central growth axis showing the annual laminae of Ach-3.

throughout the sample marked by changes in calcite fabric, alternating between brownish dense and white porous calcite layers (Fig. 2). Some growth hiatuses are apparent marking slight shifts in the growth axis. The other half of Ach-3 was milled down its long-profile using a hand-held dental drill for $\delta^{13}C$ and $\delta^{18}O$ analysis at ~0.51 mm resolution (825 samples), and trace element analysis at ~4.6 mm resolution (91 samples). Additional samples for $\delta^{13}C$ and $\delta^{18}O$ were also drilled following some individual growth layers in order to perform the “Hendy test”. The fast growth rate of individual lamina of Ach-3 (with lamina width ranging between 0.2 and 1.3 mm and average width of 0.45 mm), allows drilling of individual growth layers even at the flanks of the stalagmite. Seven samples for U-Th dating were similarly drilled using a dental drill, with samples located at the top and base of the stalagmite, on either side of possible growth hiatuses, and regularly spaced within growth phases (Fig. 2).

2.3.Geochemical analyses

Our methods follow those previously published in Asrat et al. (2007), Baker et al. (2010) and Asrat et al. (2018). A total of 825 samples for $\delta^{13}C$ and $\delta^{18}O$ analysis were milled down the long-profile of the sample. $\delta^{13}C$ and $\delta^{18}O$ were analysed at the National Environmental Isotope Facility at Keyworth, UK. The calcite samples were reacted with phosphoric acid and cryogenically purified before mass spectrometry using an Isoprime plus multiprep dual inlet mass spectrometer. The “Hendy test” samples were analysed at the University of New South Wales (UNSW, Sydney) Analytical Centre using a MAT 253 mass spectrometer using a Kiel carbonate device. By comparison with a laboratory marble standards KCM (Keyworth) and IAEA603 (UNSW), the sample $^{18}O/^{16}O$ and $^{13}C/^{12}C$ ratios are reported as $\delta^{18}O$ and $\delta^{13}C$

values in per mil (‰) versus VPDB. Analytical precisions are 0.07 ‰ for $\delta^{18}O$ and 0.04 ‰ for $\delta^{13}C$ on the standard marble (KCM) and 0.05 ‰ for $\delta^{18}O$ and $\delta^{13}C$ (IAEA603).

Trace elements were analysed from 91 powders at UNSW, Sydney. Samples of approximately 0.05 g were dissolved in 1:1 hydrochloric acid, diluted, and analysed for Ca and Mg using the PerkinElmer Optima™ 7300DV ICP-OES. Ba, Sr, Al, Cu, Fe, K, Na, P, Pb, S, Zn and U were analysed by PerkinElmer NexION 300D ICP-MS.

Seven U-Th analyses were performed in the Uranium Series Chronology Laboratory, Institute of Geology and Geophysics, Chinese Academy of Sciences. The powdered sub-samples of approximately 0.1 g were totally dissolved and spiked with a mixed ^{229}Th-^{233}U-^{236}U. Uranium and thorium fractions were separated on 2 ml anion exchange columns following standard techniques (Edwards et al., 1987). Then, the separated uranium and thorium solutions were measured on a multi-collector inductively coupled plasma mass spectrometer (MC-ICP-MS, Neptune plus). The procedures followed those described in Cheng et al. (2013).

2.4.Time series analysis

Variogram analysis on the annual growth rate time series was undertaken to determine the flickering parameter (*f*), information content (IC) and range (*r*) (Mariethoz et al., 2012). Flickering quantifies the growth rate acceleration from one year to the next through the lag-one autocorrelation of the detrended growth rate series, where 0 is no flickering (regular increases or decreases in growth rate) and -0.5 is the signal obtained from white noise. The observed flickering parameter (Mariethoz et al., 2012; Asrat et al., 2018) typically ranges between –0.5 and 0, the more negative *f* values indicating stronger flickering, interpreted as large changes in growth rate from year to year, indicative of a karst store filling and draining.

To enable such a large inter-annual variability whilst maintaining continuous deposition over hundreds of years, a sufficiently large volume karst store is hypothesised. Other statistical measures of information contained in the growth rate data are the *IC* and the *r*. *IC* quantifies the proportion of correlated signal in the time series as opposed to noise, and varies between 0% (pure noise) to 100% (noiseless correlated signal). Range (*r*) is the temporal range of the correlated part of the signal, i.e., the time over which useful information might be expected to be obtained from a growth rate time series.

Stable isotope and annual growth rate time series data were analysed for their spectral properties. Spectral analysis was performed using the SPECTRUM software for unevenly spaced paleoclimate timeseries (Schulz and Statteger, 1997). Lomb-Scargle Fourier transforms were conducted, with five windows used (Bartlett, Hanning, Rectangular, Welsh and Triangular) in order to undertake the spectral analysis of oxygen, carbon and growth rate time series, and the coherency between isotope time series. The autocorrelation of the stable isotope time series was investigated by determining the autocorrelation function.

3. Results and Interpretation

3.1.Chronology

Stalagmite Ach-3 is laminated throughout with 925 laminae. In hand-section, likely growth hiatuses with dissolution features were visually identified at lamina number 675 (growth hiatus 1) and 243 (growth hiatus 2) from the top, separating the sample into three growth phases (Fig. 2): growth phase 1 (laminae 925-676); growth phase 2 (laminae 675-244), and growth phase 3 (laminae 243-1). A third possible growth hiatus was identified near the end of the third growth phase (growth phase 3a: laminae 243-28; growth phase 3b: laminae 27-1).

The results of seven U-Th analyses are provided in Table 1. An age-depth model which confirms the three growth phases is given in Figure 3. A basal date of 10,624 ± 82 years BP constrains the initial growth phase containing 243 laminae. The six other U-Th ages occurred in stratigraphic order from 9,831 ± 68 years BP to 9,026 ± 55 years BP. The stratigraphically youngest three ages are all very similar to one another, despite the presence of possible hiatuses, suggesting that they were of short duration. The close agreement between the duration of stalagmite formation after hiatus 1 as determined by U-Th (the difference between the corrected U-Th ages ACH3-1 and ACH3-6 of 805 ± 93 years, 1σ) and the number of laminae (675 laminae) is indicative that the laminae of Ach-3 are annual in nature. This would agree with the widespread observation of annual laminae in other Ethiopian speleothems, which is due to the strong seasonality of rainfall with a distinct dry season (Asrat et al., 2007; 2018; Baker et al., 2007; 2010). Ach-3 lamina thickness has an average of 0.45 mm, and this is equivalent to the annual accumulation rate observed in Holocene and last interglacial Ethiopian stalagmites: Ach-1 (0.53 mm/yr); Bero-1 (0.45 mm/yr), Merc-1 (0.29 mm/yr); Asfa-3 (0.32 mm/yr) and GM-1 (0.44 mm/yr) (Asrat et al 2007; 2019; Baker et al 2007; 2010). We are therefore confident that the laminae are annual in nature.

Table 1. ^{230}Th dating of stalagmite Ach-3. The error is 2σ.

Sample Number	Distance from top (mm)	^{238}U (ppb)	^{232}Th (ppt)	$^{230}Th/^{232}Th$ (atomic x10^{-6})	$\delta^{234}U$* (measured)	$^{230}Th/^{238}U$ (activity)	^{230}Th Age (yr) (uncorrected)	^{230}Th Age (yr) (corrected)	$\delta^{234}U_{Initial}$** (corrected)	^{230}Th Age (yr BP)*** (corrected)
ACH3-1	0.84	1467 ±5	1904 ±38	1338.3 ±27.5	315.6 ±3.0	0.1054 ±0.0005	9074 ±51	**9045 ±55**	324 ±3	**9026 ±55**
ACH3-2	25.09	1305 ±3	1781 ±36	1294.2 ±27.3	319.5 ±2.4	0.1071 ±0.0007	9203 ±67	**9174 ±71**	328 ±2	**9155 ±71**
ACH3-3	104.74	1010 ±1	1752 ±35	1021.5 ±20.6	318.8 ±1.5	0.1074 ±0.0002	9236 ±23	**9198 ±35**	327 ±2	**9179 ±35**
ACH3-4	162.93	1299 ±2	1953 ±39	1198.5 ±25.1	311.8 ±1.6	0.1093 ±0.0007	9454 ±62	**9421 ±66**	320 ±2	**9402 ±66**
ACH3-5	231.21	1344 ±2	1827 ±37	1329.1 ±28.1	310.6 ±2.0	0.1096 ±0.0007	9491 ±68	**9461 ±71**	319 ±2	**9442 ±71**
ACH3-6	301.02	1571 ±2	4158 ±83	707.3 ±14.6	302.8 ±1.5	0.1135 ±0.0006	9908 ±54	**9850 ±68**	311 ±2	**9831 ±68**
ACH3-7	401.74	1806 ±4	4551 ±91	825.7 ±17.3	345.5 ±3.0	0.1262 ±0.0008	10697 ±73	**10643 ±82**	356 ±3	**10624 ±82**

*$\delta^{234}U = ([^{234}U/^{238}U]_{activity} - 1)$x1000. **$\delta^{234}U_{initial}$ was calculated based on ^{230}Th age (T), i.e., $\delta^{234}U_{initial} = \delta^{234}U_{measured}$ x $e^{\delta 234xT}$.
Corrected ^{230}Th ages assume the initial $^{230}Th/^{232}Th$ atomic ratio of 4.4 ±2.2 x10^{-6}.
Those are the values for a material at secular equilibrium, with the bulk earth $^{232}Th/^{238}U$ value of 3.8. The errors are arbitrarily assumed to be 50%.
***B.P. stands for "Before Present" where the "Present" is defined as the year 2000 A.D.

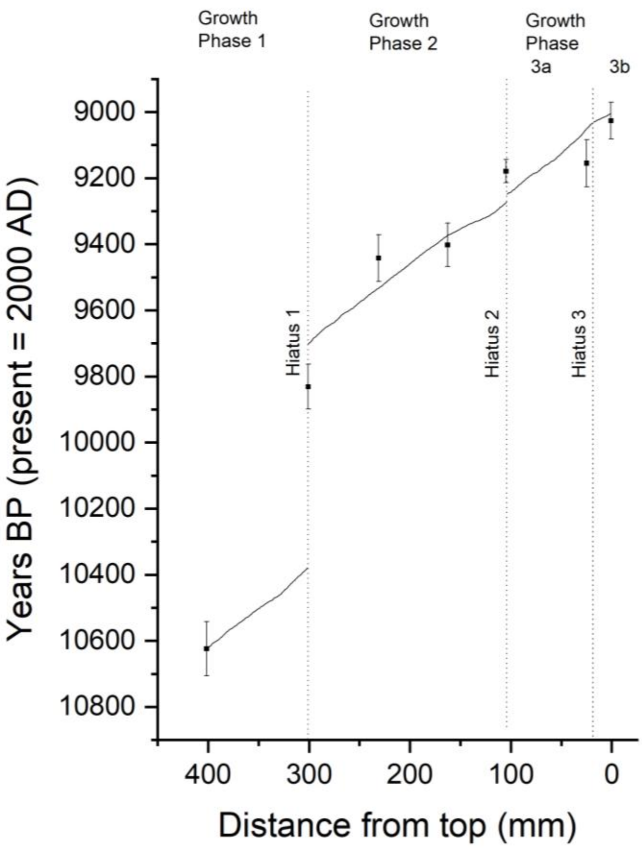

Figure 3. An age depth model for Ach-3. Depth measured as distance (mm) from the top of the speleothem. Locations of ages and hiatuses are marked.

3.2. Geochemical proxies

The 825 $\delta^{13}C$ and $\delta^{18}O$ analyses are presented in Figure 4A as scatter plots of oxygen vs carbon isotopes down the growth axis, as well as for analyses made along six growth laminae (Fig. 4B) equivalent to the classic ‘Hendy test’ (Hendy, 1971). Figure 4A shows that the two isotopes are positively correlated along the growth axis in all growth phases except for growth phase 2, and Figure 4B shows that the two isotopes are positively correlated along all sampled growth laminae, including those in growth phase 2. This correlation between $\delta^{13}C$ and $\delta^{18}O$ is similar to other Ethiopian stalagmites (Asrat et al., 2007; 2018; Baker et al., 2010), and demonstrates that deposition is not in equilibrium (Fantadis and Ehhalt, 1970; Mickler et al., 2006; Wiedner et al., 2008). The gradient of $\delta^{13}C/\delta^{18}O$ is between 3.0 and 3.5

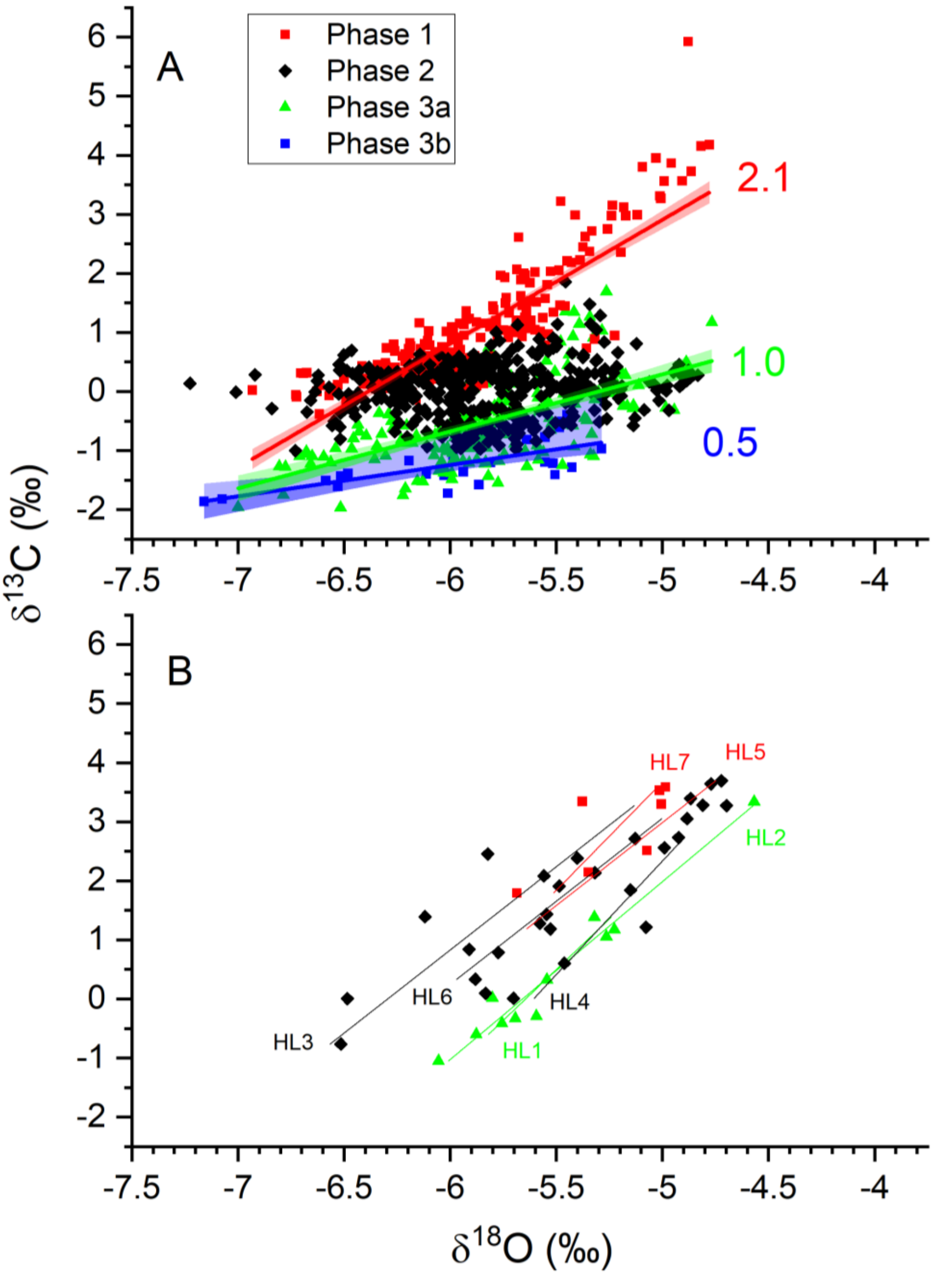

Figure 4. Scatter plots of $\delta^{18}O$ vs $\delta^{13}C$ (A) for each growth phase (B) 'Hendy' tests along growth laminae in stalagmite Ach-3. Note that similar dis-equilibrium deposition was observed in Ach-1 and Bero-1 (Asrat et al., 2007; Baker et al., 2010).

along growth laminae, and for growth phases 1, 3a and 3b is 2.1, 1.0 and 0.5, respectively, with no correlation between $\delta^{13}C$ and $\delta^{18}O$ in growth phase 2. These gradients observed in stalagmite Ach-3 are similar to the mean value of the gradient of $\delta^{13}C/\delta^{18}O$ of 3.8 observed along vertical transects and 3.9 observed spatially across calcite deposited on glass plates by Mickler et al. (2006). These were attributed to kinetic fractionation during non-equilibrium deposition due to ^{18}O and ^{13}C Rayleigh-distillation enrichment in the HCO_3^- reservoir during progressive CO_2 degassing and calcite precipitation. They are also similar to the gradient of $\delta^{13}C/\delta^{18}O$ of 1.4 ± 0.6 for the fast-degassing of CO_2 in carbonate precipitation experiments (Wiedner et al., 2008). Though the classic "Hendy test" might not be conclusive in predicting the equilibrium or non-equilibrium deposition of calcite (e.g., Dorale and Liu, 2003), our cave monitoring and modern speleothem records from the Mechara caves further confirm that non-equilibrium deposition is likely for Ach-3. The lowest values of the predicted equilibrium calcite $\delta^{18}O$ variations from measured modern drip water $\delta^{18}O$ data in various caves in the region are not observed in speleothem $\delta^{18}O$ records, indicating non-equilibrium deposition of calcite (Baker et al., 2007; Asrat et al., 2008). However, in Ach-3 we note a trend over time in the $\delta^{13}C/\delta^{18}O$ gradient, and extent of non-equilibrium deposition. In the last years of deposition (Phase 3), the gradient is 1.0 (Phase 3a) and 0.5 (Phase 3b), which could indicate a change in the extent or type of isotope fractionation, for example additional evaporative fractionation due to slower drip rates, and / or increased kinetic fractionation due to increased drip water pCO_2.

Trace element data for the 91 samples is presented in Supplemental Table 1. Elements were normalised to calcium and analysed using PCA (Supplemental Figure 1). Three components explained 80 % of the variability in the data. PC1 (36 % of the variance explained) correlated with the elements P, Na, K and Zn; PC2 (22 % of the variance explained) correlated with Mg, Sr, and U; and PC3 (22 % of the variance explained) correlated with Fe, Al, Ba and Pb. We interpret PC1 as soil or cave sediment derived elements, given the presence of nutrients and organic-associated metals (Borsato et al., 2007; Hartland et al., 2012). PC2 is interpreted as bedrock-derived dissolution elements, and PC3 as elements derived from sediment, colloidal and particulate material (Borsato et al., 2007). Time series of the three principal components shows that all three components have high scores at the start of growth, and decline over the first growth phase (Supplemental Figure 2). PC2 then has a long-term decrease over the rest of the period of deposition, indicative of a decrease in bedrock-derived metals over time (Supplemental Figure 2). PC1 increases to its highest value, and PC2 increases by a lesser amount, over the last years of deposition, while at the same time PC3 decreases to its lowest score.

The time series for $\delta^{13}C$ and $\delta^{18}O$ are presented in Figure 5, together with representative trace element data for PC1 (P/Ca) and PC2 (Sr/Ca, Mg/Ca) and annual growth rates. The 825 isotope analyses represent an approximately annually resolved record. In the first deposition phase, from ~10,600 – ~10,350 BP, there is a trend towards lower ratios in Mg/Ca, Sr/Ca, and more negative $\delta^{18}O$, indicative of generally increasingly wetter conditions or a shorter vadose zone water residence time. The observation of higher concentrations of soil or cave sediment derived elements such as P at the start of deposition agrees with the observation of detrital material in the bottom few growth laminae, likely derived from cave sediments, as well as the subsequent flushing of soluble elements from the soil and vadose zone at the start of the growth phase.

Stalagmite deposition from ~9,700 to ~9,000 years BP in growth phases 2 and 3a has a long-term trend to more negative $\delta^{13}C$ and lower Sr/Ca and Mg/Ca. This could be indicative of the continuation of the trend to increasingly wetter conditions or a shorter vadose zone water residence time and decreasing prior calcite precipitation along the flow path over this period (Fairchild et al., 2000). Growth rates and oxygen isotope composition exhibit no long-term trend, instead have multi-decadal variability.

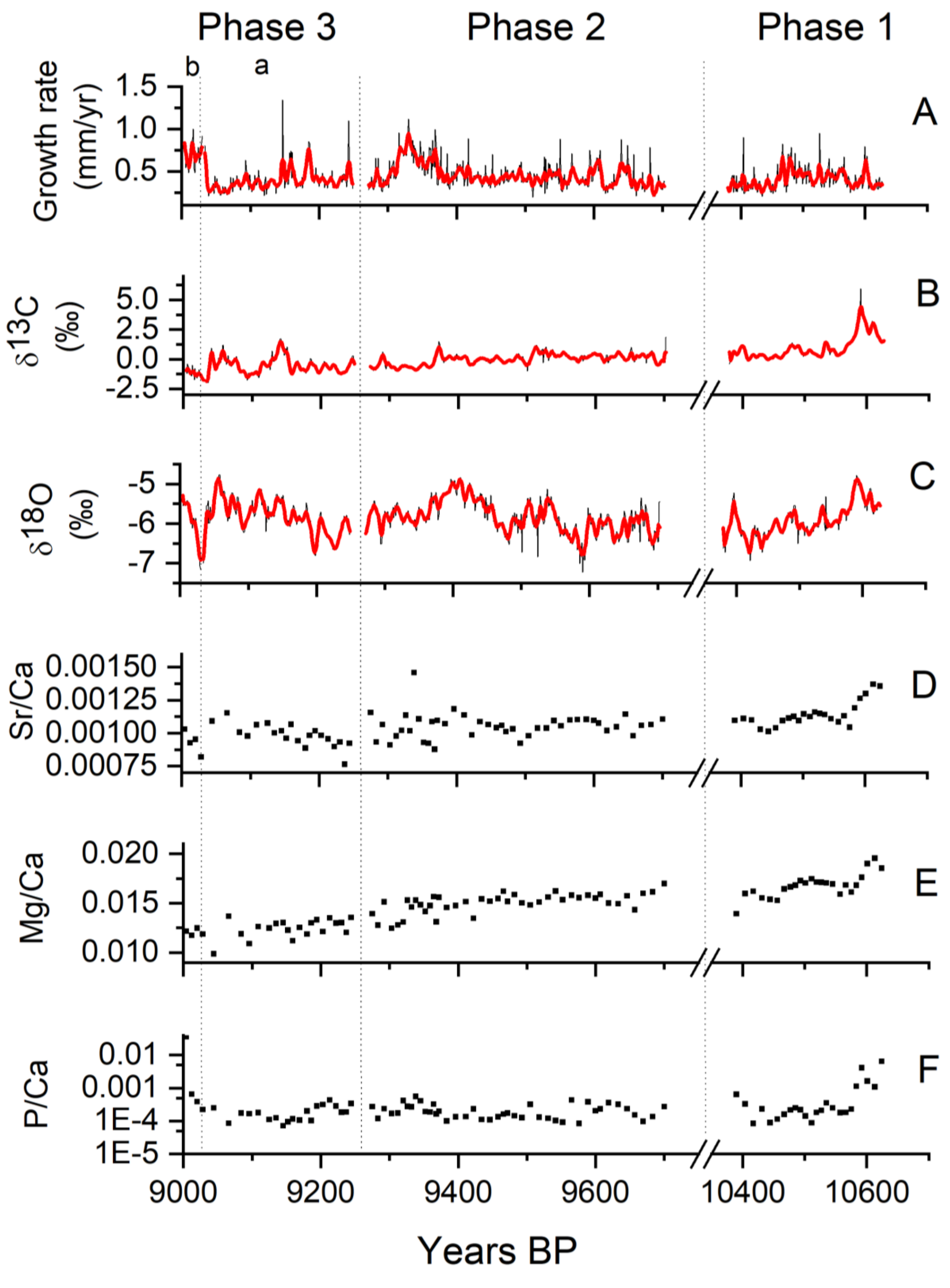

Figure 5. Time series of growth rate and geochemical proxies in Ach-3. (A) Annual growth rate, (B) $\delta^{13}C$, (C) $\delta^{18}O$, (D) Sr/Ca, (E) Mg/Ca, (F) P/Ca.

Geochemical and isotope data are unchanged over the possible short-duration growth phase 3b at ~9300 BP. However, over this last 28 years of deposition, geochemical trends reverse, with increasing PC1 and decreasing PC3 in the last years of deposition (Supplemental Figure 2), increases in Sr, Mg, and $\delta^{18}O$, and an increase in growth rate. A change in geochemical, growth rate and isotopic trends has been observed previously at the end of stalagmite deposition during Middle and Late Holocene (Asrat et al., 2007; 2018) and interpreted as a change in hydrological regime as the hydroclimate dries, e.g. disconnection from the soil water store or decrease in fracture flow component. In these records, the role of active tectonics in controlling speleothem growth duration by changing the flow regimes has been identified.

The mean $\delta^{18}O$ composition of the Early Holocene Ach-3 (-5.86 ± 0.42‰) is more negative compared to all other modern (Merc-1: -1.22 ± 0.31‰; Asfa-3: -1.37 ± 0.37‰; Baker et al., 2007), and Middle to Late Holocene (Bero-1: -3.42 ± 1.45‰, Baker et al. 2010; Ach-1: -3.20 ± 0.35‰, Asrat et al., 2007) samples from the region. All the published stalagmite records have evidence of non-equilibrium deposition. Assuming a similar extent of disequilibrium in all the stalagmites, including Ach-3, it indicates that drip water was ~2‰ more negative in the Early Holocene (Ach-3: -5.86 ± 0.42‰) compared to that of Middle Holocene (Ach-1: -3.20 ± 0.35‰; Bero-1: -3.42 ± 1.45‰).

3.3. Time series analysis

A summary of the results of spectral analysis on both stable isotopes and growth rate time series, and variogram analysis and flickering of growth rate time series, is presented in Table 2. Full spectral analysis results are presented in Supplemental Table 2 and Supplemental Figure 3, and autocorrelation plots in Supplemental Figure 4.

Variogram analysis of growth rates time series suggests this is a stalagmite with a relatively short time period where there is useful climate information in the growth rate data.

Table 2. (A) variogram analysis for stalagmite Ach-3 for the three growth phases (phase 1 – oldest; phase 3 – youngest): range *r*; information content IC; flickering *f*. (B) Summary of geostatistical properties for Ach-3, Bero-1 and Ach-1: univariate spectral analysis, showing the dominant and statistically significant periodicities in the oxygen isotope, carbon isotope and growth rate time series. Oxygen and carbon isotope time series have coherent periodicities at 15-16 years (Ach-3), 16-17 and 25 years (Bero-1) and 16-17 years (Ach-1). Summary variogram statistics r and f.

(A) Variogram analysis for stalagmite Ach-3

Phase 3: 28-243	Phase 2: 244-675	Phase 1: 676-925
r = 12.1 years	r = 28.4 years	r = 13.0 years
IC = 66.7%	IC = 64.3%	IC = 50.5%
f = -0.34	*f* = -0.38	*f* = -0.26

(B) Geostatistical summary for Ach-3, Bero-1 and Ach-1 (period in years)

Statistically significant periodicities (years)				Variogram Analysis	
	$\delta^{18}O$	$\delta^{13}C$	Growth rate	*r*	*f*
<u>Ach-3</u>					
~9.2 ka	18-25	19-21	>=*r*	13	-0.26
~9.4 ka	17-18	19-21	11	28	-0.38
~10.4 ka	25-30	19-23	>=*r*	12	-0.35
<u>Bero-1</u>					
~4.3–4.2 ka	8, 13, 26-28	8, 13, 16-17, 26-28	11–15, 17–21	6	-0.36
~5.4–5.2 ka	16-20	18-21, 26	10–13, 15–20	>*	-0.74
~7.8–7.5 ka	28-30	21, 27-30	11–13, 18–19	335	-0.51
<u>Ach-1</u>					
~5.1–4.7 ka	18–21	18-19	18–21	80	-0.36

These are the range, *r*, = 28 years in growth phase 2, and a much shorter range of *r* = 12-13 years in growth phases 1 and 3 (Table 2A). The *r* values are low compared to a global analysis of the growth rates of laminated stalagmites in Mariethoz et al. (2012) and Baker et al (2021), but similar to other Ethiopian samples. The information content, *IC*, in the growth rate time series ranges from 0.50 to 0.67, highest and relatively similar in growth phases 2 and 3. An *IC* over 50% means that the stalagmite growth rate data contains significant useful signal. An *IC* >50% and *r*<150 years classifies Ach-3 as a ‘’Type A’’ stalagmite of Mariethoz et al. (2012), which is likely to be suitable for interpreting multi-decadal information, with the higher *IC* in phases 2 and 3 suggesting that these are less noisy. The presence of flickering, *f*, of -0.26 (phase 1), -0.37 (phase 2) and -0.34 (phase 3), is indicative of a water filled store supplying the stalagmite of sufficient volume to maintain continuous deposition for at least several decades, with hydrologically-controlled year-by-year variations in water level controlling inter-annual growth rate variations. Phase 1 of deposition has a lower *IC* and relatively short range, and suggests that the first growth phase contains the least climate information.

Inspection of the autocorrelation of $\delta^{13}C$ and $\delta^{18}O$ time series for each growth phase (Supplemental Figure 4) shows that the autocorrelation for both stable isotopes is similar to each other for growth phases 1 and 3. Between growth phases, there is a slight decrease in autocorrelation from growth phase 1 to growth phase 3, and a slight decoupling of the $\delta^{13}C$ and $\delta^{18}O$ autocorrelation functions in growth phase 2. If soil processes were the dominant control on speleothem $\delta^{13}C$, a stronger autocorrelation in $\delta^{13}C$ compared to $\delta^{18}O$ might be expected. This is not observed in Ach-3. The lower autocorrelation of $\delta^{13}C$ compared to $\delta^{18}O$ in growth phase 2 agrees with the observed lack of correlation between $\delta^{13}C$ and $\delta^{18}O$ through time in growth phase 2, and a possible decrease in the extent or type of isotope fractionation in this phase. Overall, the similarity in the autocorrelation functions of $\delta^{13}C$ and

$\delta^{18}O$, combined with the evidence of isotope fractionation from the correlation between $\delta^{13}C$ and $\delta^{18}O$ over time and along growth layers, suggests the dominant control of in-cave isotope fractionation processes on the composition of both $\delta^{13}C$ and $\delta^{18}O$, strongest in growth phases 1 and 3.

Spectral analysis on the $\delta^{18}O$, $\delta^{13}C$ and growth rate time series is presented in Table 2B and Supplemental Figure 3. There are similar and consistent periodic components in the $\delta^{13}C$ and $\delta^{18}O$ time series at around 15-25 years and 19-25 years in all three growth phases. Bivariate analysis of $\delta^{13}C$ and $\delta^{18}O$ demonstrates a coherency at 16-17 years. In growth phases 1 and 3, these periodic components in the stable isotope time series occur at time periods greater than the value of *r* obtained from the growth rate data, suggesting an independent forcing mechanism is dominant. Evidence that isotope fractionation is occurring during deposition, and that this is likely to be from within-cave fractionation processes, suggest that within-cave isotope fractionation processes are the dominant driver of the observed multi-decadal periodicity in the stable isotope time series. These within-cave isotope fractionation processes can be climatically forced, and we cautiously interpret these spectral frequencies as representative of an indirect hydroclimatic forcing affecting in-cave isotope fractionation processes. Spectral analysis on the growth rate timeseries demonstrates that there are no periodic signals shorter than the range, *r*, for all growth phases (Table 2B). Table 2B also presents the results of previously published spectral analyses on Holocene Ethiopian stalagmites, demonstrating a consistent multidecadal periodic signal in $\delta^{18}O$ time series between different time periods and different caves.

4. Discussion

4.1.Conceptual growth model

Stable isotope and trace element geochemical data and geostatistical analyses, combined with our hydrogeological understanding of the unsaturated zone properties of the limestone (Asrat et al., 2007), suggest that stalagmite Ach-3 is fed by a mixture of diffuse flow, through porous limestone and calcareous mudstone, as well as solutionally enlarged fractures. The latter are relatively small in volume and more important than diffuse flow contributions, as indicated by the 28-year range in growth rate time series. This is indicative of a relatively small water store which controls growth rate variability through limits on the extent of prior calcite precipitation (PCP) in the fracture, and can determine drip rate. Considering the whole period of stalagmite formation, trace element data identifies an initial sediment or soil-derived elemental signal, potentially indicative of an initial flush of trace elements from the soil or interactions with cave sediments, and a loss of this elemental signal in the last decade of deposition. The duration of this last growth phase is the same as the range in the variogram analysis of growth rate and consistent with the inferred small water volume of the karst fracture. $\delta^{13}C$ and $\delta^{18}O$ have very similar autocorrelation functions, have coherent, periodic signals in the timeseries, and strongly correlate between $\delta^{13}C$ and $\delta^{18}O$ along growth laminae and within growth phases. This indicates a common control on both isotopes of within-cave isotope fractionation. Multidecadal variability in stable isotopes is therefore due to changes in the extent of isotope fractionation, either through kinetic or disequilibrium fractionation processes, such as changes in drip rate or drip water calcite saturation that control the extent of ^{18}O and ^{13}C enrichment in the HCO_3^- water film during progressive CO_2 degassing and stalagmite precipitation (Mickler et al., 2006; Scholz et al., 2009).

We present a conceptual model of the hydrogeochemistry associated stalagmite growth in Figure 6. In growth phase 1, there is an initial input of soil or sediment derived material.

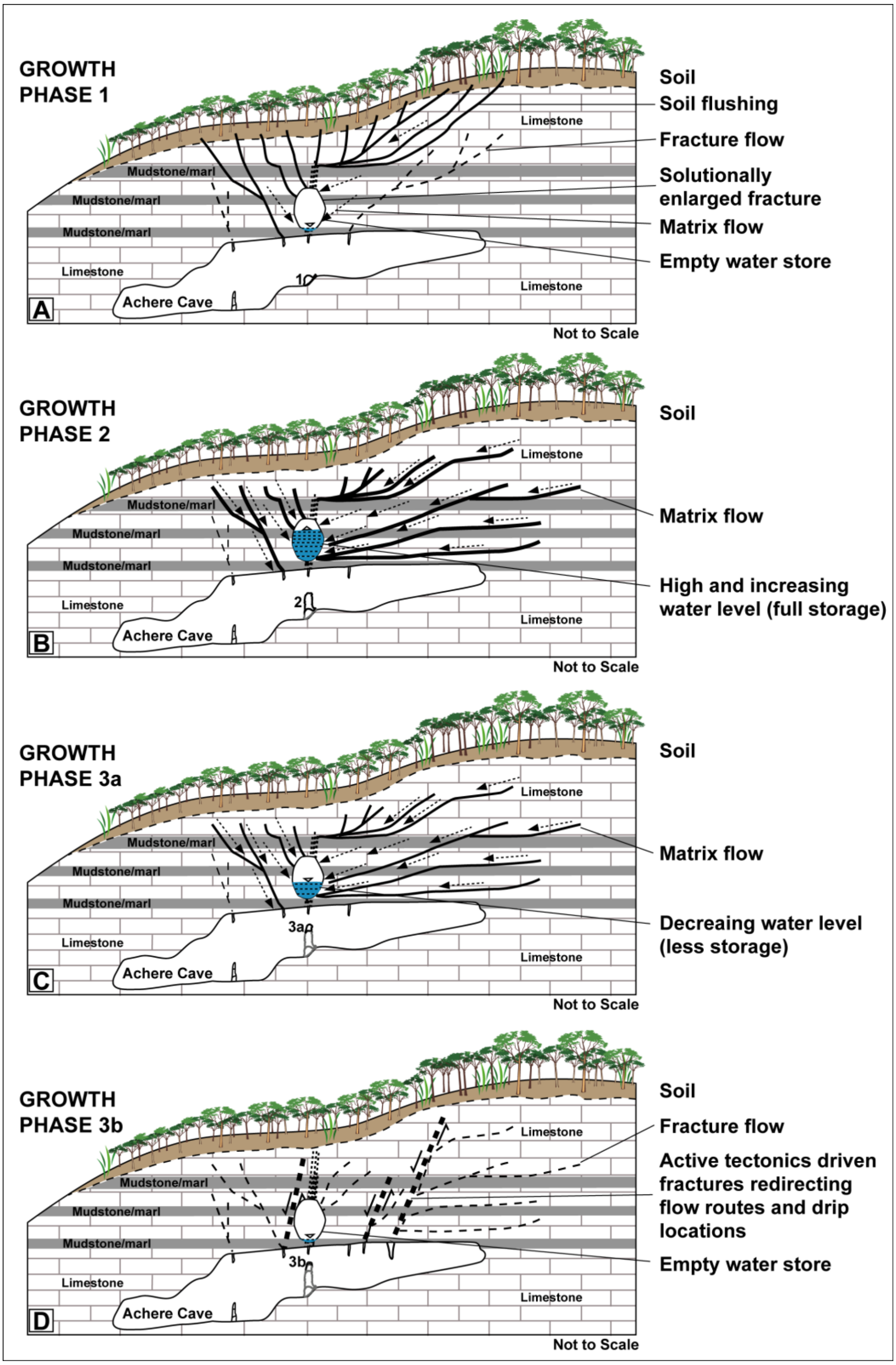

Figure 6. Conceptual model for the deposition of stalagmite Ach-3: (A) Growth phase 1: initiation and flushing from soil dominating the flow; (B) Growth phase 2: wet and continuous growth from full storage, with multi-decadal variability due to within cave processes (such as drip rate or water saturation); (C) Growth phase 3a: similar flow conditions to that of phase 2 but with less water storage; and (D) major tectonic process leading to the redirecting of flow regimes and relocation of drip sources leading to rapid shutoff and growth cessation. Cartoons modified from Asrat et al. (2007; 2018).

There is a low information content in the growth rate time series in this growth phase, indicating a relatively noisy signal due to the combination of growth rate controls from the initial flush of soil-derived material as well as a hydrological control. The periodic signal in the growth rate time series and range are identical, at ~12 years, suggesting relatively limited water storage to the stalagmite during this growth phase (indicated by an empty reservoir in Fig. 6A). In growth phase 2 the best information content and largest range is observed, which we interpret as the karst store relatively full of water (full storage reservoir in Fig. 6B) compared to other growth phases. Decreasing Sr/Ca and Mg/Ca ratios over this growth phase further indicate increasing water availability. In this growth phase the $\delta^{13}C$ and $\delta^{18}O$ data show some evidence that isotope fractionation processes have less dominant control on isotopic composition than in the other phases. In growth phase 3a, the range in the growth rate time series analysis decreases, but all other proxies are identical to phase 2 and indicative of persisting high water availability (half storage reservoir in Fig. 6C). Throughout these growth phases there is a consistent multidecadal variability in $\delta^{13}C$ and $\delta^{18}O$, which is interpreted as being forced by non-equilibrium deposition processes. Finally, in phase 3b, we have a 28-year period of deposition where trace element data indicates a decrease or loss of soil connectivity. This results in an increase in growth rate until growth cessation (an empty reservoir in Fig. 6D). Given the preceding growth indicated progressive increases in water availability, we infer that tectonic activity disrupted the water flow path to the stalagmite between growth phases 3a and 3b.

4.2. Non-equilibrium deposition and multidecadal variability in $\delta^{18}O$

Spectral analyses on $\delta^{18}O$ for the three stalagmites: Ach-3, and the previously published Bero-1, and Ach-1, demonstrate a multidecadal variability through the Holocene (Table 2 and

Supplemental Figure 5). The amplitude of this variability is ~1 ‰. The dominant statistically significant frequencies are between 13 and 30 years. We observe spectral frequencies in this range in stalagmites from different sites with different hydrogeology and flow paths. This multi-decadal variability in $\delta^{18}O$ can (i) derive from water isotope fractionation process, including partial evaporation of soil and shallow epikarst water, and within-cave fractionation due to changes in the extent of isotopic dis-equilibrium during stalagmite formation (drier and increased drip water pCO_2 = more positive isotopic composition), and (ii) in cases with limited water mixing and a fast flow component to the hydrology, a signal from $\delta^{18}O$ of precipitation or recharge (wetter = more negative) (Fig. 7). Our evidence base is:

(1) there is a relatively small seasonal variability in the modern $\delta^{18}O$ of precipitation. Baker et al. (2010) presented IAEA data from Addis Ababa which show that the isotopic composition of precipitation in July and August, the peak of the summer (‘big’) rains, has $\delta^{18}O$, which is more negative than April ‘small’ rains by ~3 ‰. Low rainfall amounts during the small rains could therefore lead to more negative recharge water $\delta^{18}O$, but as the small rains typically represent just 25-35 % of total annual rainfall, with a total range of 15-43 % (data from 20 years of complete data since 1984, Bedessa meteorological station, see Fig. 1), any effect is expected to be less than ~1.2 ‰ in annual weighted mean isotopic composition of precipitation (Fig. 7, process ‘A’).

(2) Recharge waters will likely mix with water of different ages, depending on the flow path and the presence and volume of any subsurface karst water stores, such as solutionally enhanced fractures. Where well-mixed water from a single store is the source of drip water, and no soil or epikarst evaporation is significant, there will be a more negative $\delta^{18}O$ signal deriving from the precipitation $\delta^{18}O$. Any changes in the

annual mean δ^{18}O of precipitation due to changes in the relative proportion of small and big rains (see point 1) will be decreased in amplitude due to the mixing of waters (Fig. 7, process ‘C’).

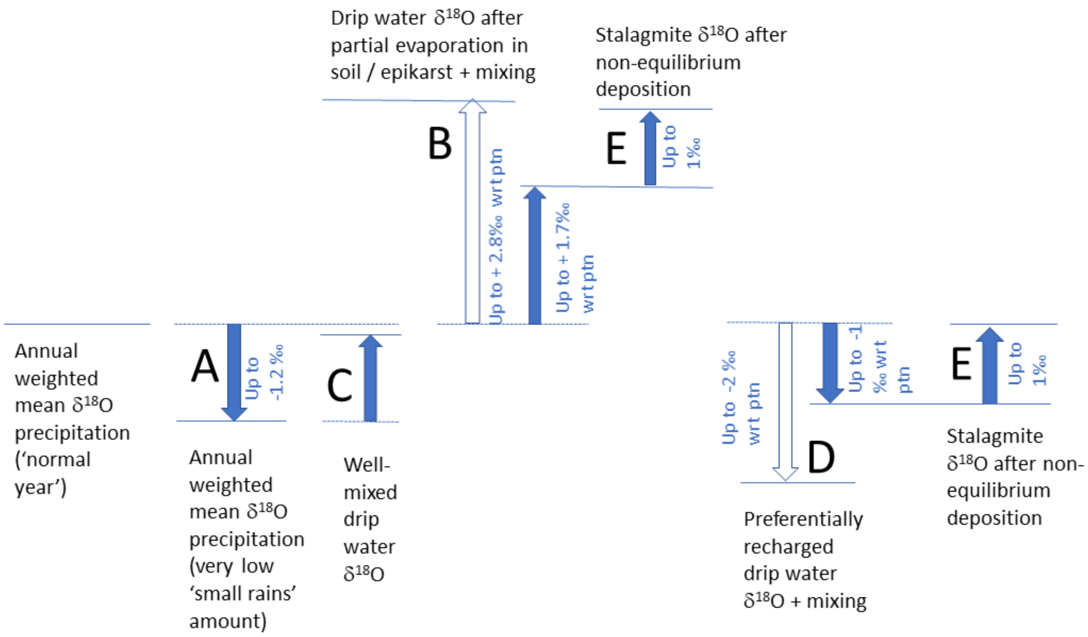

Figure 7. Isotope composition conceptual diagram. The changes in oxygen isotope composition are based on observed Addis Ababa IAEA monthly δ^{18}O precipitation (Process A); observed global range of epikarst and soil evaporative fractionation(open arrow) and range for P/PET = 0.9 (filled arrow) (Baker et al., 2019) (Process B); well-mixed drip water δ^{18}O (Process C); observed global range of recharge bias (open arrow) and range for P/PET = 0.9 (filled arrow) (Baker et al., 2019) (Process D); and modelled non-equilibrium fractionation factors (Scholz et al., 2011) (Process E).

(3) A single mixed store is a simplification of actual karst hydrology where multiple water flow paths are more common (Tooth and Fairchild, 2003; Fairchild et al., 2006; Hartman and Baker, 2017), e.g. an additional fracture or by-pass flow which allows a fast flow, less mixed flow component (Fig. 7, process ‘D’). In these instances, a recharge-bias in the δ^{18}O signal may be preserved in the drip water δ^{18}O. In the global meta-analysis of global dripwater δ^{18}O, Baker et al. (2019) demonstrated drip waters which were up to 2 ‰ more negative than the annual mean of precipitation, most commonly observed in regions with very distinct wet seasons in otherwise water-limited environments. P/PET in the Mechara region is calculated to be 0.86

(FAO New_LocClim) or 0.88 (Wagari Furi, 2005), and for an equivalent P/PET in the global analysis of dripwater $\delta^{18}O$, cave drip waters in the Mechara region might be expected to be up to 1 ‰ more negative than the annual mean of precipitation due to selective recharge. In-cave fractionation processes could operate in the opposite direction to this effect (see point 5 below).

(4) Precipitation that contributes to the soil water store, and in some cases the shallow epikarst water, can undergo evaporation, leading to the remaining water $\delta^{18}O$ becoming increasingly isotopically positive (Cuthbert et al., 2014). Partially evaporated water may be subsequently recharged to the cave, having a more positive $\delta^{18}O$ than the original precipitation. In a global meta-analysis, Baker et al. (2019) identified the presence of drip water that was exceptionally up to +2.8 ‰ compared to weighted mean precipitation $\delta^{18}O$, and for water limited environments with P/PET similar to the Mechara region, up to + 1.7 ‰. Partially evaporated $\delta^{18}O$ has previously been hypothesised as forming part of the $\delta^{18}O$ in an Ethiopian stalagmite (Baker et al., 2010), where forward modelling for the modern growth phase of the Bero-1 stalagmite identified a positive isotope offset of 2.0 to 2.5 ‰, attributed to evaporative fractionation processes between rainfall and the stalagmite (Fig. 7, process 'B'). However, the effect of possible changes in the relative proportion of small and big rains on the partial evaporation of soil or epikarst waters is unclear. For example, if the small rains led to the recharge of more partially evaporated water than the big rains, due to relative low rainfall amounts in the former, then relatively dry small rain seasons could lead to more negative drip water $\delta^{18}O$.

(5) All stalagmites analysed in Ethiopia to date, demonstrate conclusive evidence of non-equilibrium deposition. In Ach-3, there is strong correlation between $\delta^{13}C$ and $\delta^{18}O$ along growth laminae and over time, with $\delta^{13}C/\delta^{18}O$ gradients < 3. Bero-1 and Ach-1

also had $\delta^{13}C/\delta^{18}O$ gradients <3. The similar range in $\delta^{13}C/\delta^{18}O$ gradients of the three stalagmites to laboratory experiments (Wiedner et al., 2008) and the meta-analysis and field observations of Mickler et al. (2006), combined with the strong correlations between $\delta^{13}C$ and $\delta^{18}O$ for each stalagmite, and similar and coherent multidecadal spectral frequencies between $\delta^{18}O$ and $\delta^{13}C$, suggests a dominant in-cave control. One such mechanism is a change in drip rate which controls disequilibrium isotope fractionation during the progressive degassing of CO_2 from the water film during stalagmite formation (Fig. 7, Process 'E'). All three stalagmites have similar amplitude in multidecadal signal (up to ~1 ‰). The iSOLUTION model of oxygen and carbon isotope composition of stalagmite calcite (Scholz et al., 2009; Deininger and Scholz, 2019) models disequilibrium isotope fractionation processes, and produces this magnitude of oxygen isotope fractionation for high pCO_2 drip waters and relatively slow drip rates. Kinetic isotope fractionation due to rapid degassing from high pCO_2 drip waters could also lead to this magnitude of isotope fractionation for faster drip rates (Mickler et al., 2006, Wiedner et al., 2008) and would be considered likely given the fast growth rates of Ethiopian stalagmites.

We provide multiple lines of evidence that the multidecadal variability in stalagmite $\delta^{18}O$ in Ethiopian stalagmites is likely due to the karst hydrological processes on water mixing, with preferential recharge and isotope fractionation processes operating with opposite signs in $\delta^{18}O$ from the same climate forcing as visualised in Figure 7. We hypothesise that inter-annual variability in the relative amounts of small and big rains may have some influence on the mean annual precipitation $\delta^{18}O$. However, cave drip water $\delta^{18}O$ is further altered by the effects of variable karst hydrology and water isotope fractionation processes, leading to a cave drip water isotopic signature that represents a combination of precipitation $\delta^{18}O$, preferential recharge $\delta^{18}O$ and / or a $\delta^{18}O$ that represents the extent of partial evaporation of the water. In years of decreased recharge, this in turn potentially leads to decreases in drip rate to the stalagmites, leading to the potential of increased isotope fractionation due to disequilibrium deposition. Decreases in drip rate do not necessarily have a linear relationship with surface hydroclimate forcing, due to the non-linear nature of karst hydrology and mixing of waters in karst stores and fractures. Our observation of multidecadal spectral frequency in $\delta^{18}O$ is therefore likely to be due to individual extremes of dry years, which determine the volume of recharge to these karst stores, and in turn the drip rate from the store, including both the mean annual drip rate and /or the duration of dripping in one year. Superimposed on this signal could also be evaporative fractionation of water in the soil, shallow vadose zone or in the cave, and / or a preferential recharge signal, both of which operate with the opposite sign. With drier conditions, in-cave isotope fractionation and evaporative fractionation effects operate with the same sign, increasing drip water $\delta^{18}O$ due to increased evaporation at the same time as disequilibrium deposition increased with lower drip rates. However, for some samples with a fast-flow or bypass-flow component, preferential recharge could be significant in controlling drip water $\delta^{18}O$, and this signal could dominate over fractionation processes and generate a multi-decadal signal with the opposite sign. Superimposed on all flow types is the possibility of kinetic isotope fractionation due to high drip water pCO_2, which is likely given the very fast growth rates of Ethiopian stalagmites.

The modern East African monsoon is connected to the larger Indo-Pacific-Asian monsoon, as the annual formation of the South Asian monsoon generates trade winds in the eastern Indian Ocean and eastern Africa, and associated moisture and rainfall in Ethiopia (Vizy and Cook, 2003; Funk et al. 2016). These moisture patterns are further modulated by the strength of the Indo-Pacific warm pool heating, through multi-decadal climate phenomena including ENSO, IOD and the Pacific Decadal Oscillation (PDO). Hence, it is useful to compare the multidecadal variability in $\delta^{18}O$ in Early to mid-Holocene Ethiopian stalagmites to records of similar temporal resolution and growth periods in the broader Indo-Pacific-Asian monsoon region. For example, high-resolution north Chinese stalagmite $\delta^{18}O$ records over the last 2000 years (Zhang et al., 2019) suggest a strong Indian Ocean influence on stalagmite multidecadal $\delta^{18}O$ variability, with a more distal moisture source leading to more negative $\delta^{18}O$ precipitation during La Niña events.

We identified three suitable high-resolution stalagmite records for comparison (Table 3). In Southern Oman, the Qunf Cave Q5 record of Fleitmann et al (2003) deposited over the period 8.0 to 2.7 ka had spectral peaks at 10.9 and 10.2 years, noting the sampling resolution for $\delta^{18}O$ was 2-15 yr. In Northern Oman, Neff et al (2001) sampled at 1.4 yr resolution from around 8.4 to 7.9 ka and identified multidecadal peaks in $\delta^{18}O$ in their untuned record at 3.3, 4.9, 7.3, 35 and 78 years. In southern inland China, Dykoski et al (2005) report an annual resolution record from 8250 – 8110 years BP with peaks at 2.3 – 2.4, 4.8, 5.1, 6.4, 6.6 and 44 years. Disregarding spectral peaks that are close to the sampling resolution of each of these records, a comparison between Ethiopian, Oman and central China stalagmite $\delta^{18}O$ in the Early Holocene suggests that there are different multi-decadal $\delta^{18}O$ signals in the Early Holocene in Ethiopia, Oman and China. Additional annual or near-annual resolution $\delta^{18}O$ records would be of benefit to ascertain if this is due to regional climate differences in the multidecadal forcing of $\delta^{18}O$ within the monsoon region, regional differences in the strength of climate influence on precipitation $\delta^{18}O$, and/or the relative importance of karst hydrological variability.

Furthermore, the precipitation $\delta^{18}O$ record from the only long-term monitoring station at Addis Ababa shows that there is little seasonal variability in $\delta^{18}O$ (e.g., Baker et al., 2010). A recent study by Bedaso et al. (2020) on $\delta^{18}O$ and $\delta^{2}H$ of precipitation samples collected at daily, weekly and monthly intervals in different parts of Ethiopia representing local climate

Table 3. Comparison of the $\delta^{18}O$ record of Ach-3 with Holocene speleothems from Oman and China.

Speleothem	**Location**	**Periodicity (yrs)***	**Growth period**	**Reference**
Qunf Cave, stalagmite Q5, 0.7 mm sampling resolution = 2 - 15 yr resolution	Southern Oman	~220, ~140, ~107, *10.9, 10.2* (90% red noise)	8.0 – 2.7ka	Fleitmann et al. (2003)
Hoti Cave, stalagmite H5, high resolution section: 0.4 mm = 1.4 yrs	Northern Oman	78, 35, 7.3, *4.9, 3.3* (90% red noise)	~7.9 – 8.4ka	Neff et al. (2001)
Dongge Cave, high resolution section: ~1 yr /sample	Southern inland China	44, 6.6, 6.4, 5.1, 4.8, *2.4-2.3*	8110 – 8250 yrs BP	Dykoski et al. (2005)

**Italics indicates close to sampling resolution;* significance level shown where reported.

regimes confirmed the weak correlation between rainfall amount and $\delta^{18}O$ values of precipitation. The same study further indicated the absence of discernible source region variability among the different stations. The mean moisture back-trajectory paths show the Mechara caves on the Southeastern Ethiopian highlands receive most of their moisture from the southwestern and northern Indian Ocean, on southerly and easterly wind trajectories, respectively. Hence, the different multi-decadal variabilities in the Ethiopian stalagmites cannot be explained by moisture source variability alone.

4.3. The role of tectonics

The MER and the adjacent highlands have been tectonically and seismically active since the Mid-Miocene (Gouin, 1979; Ayele and Kulhánek, 2000; Corti, 2009; Ayele, 2017). The rift-related extensional tectonics led to the initiation and further development of the Achere-Aynage cave system where conduits developed following NE-SW oriented fractures, while the zone of conduit development was restricted by the mudstone/marl horizons (Asrat et al., 2008). The aquifer architecture and hydrological flow regimes above the caves are therefore a strong reflection of this tectonic-lithological interaction, which has been changing through time, even within the time frame of a single speleothem growth. Active tectonics in many cases is responsible for developing and continuously modifying the fracture systems which usually refocused groundwater flow paths along newly formed or reactivated fractures and conduits, in many cases leading to the cessation of growth of speleothems, manifested in growth hiatuses (Asrat, 2012).

In addition to frequent growth hiatuses, the control of seismicity on speleothem growth in the Mechara caves is manifested in: (i) frequent anomalous laminae such as those containing higher proportion of impurities corresponding to known earthquake events; (ii) frequent deviations from vertical growth axis which can be attributed to shifting of the drip location; and (iii) upward thinning stalagmites which show in many cases abrupt change from regular ‘candlestick” shape implying a regular flow regime to upward thinning shape which could indicate the release of water from a karst store after a seismic event (Asrat, 2012).

Though seismicity data for the region are scarcely available for the period prior to the 20th century (Gouin, 1979), several studies in the MER show that tectonic activities particularly intensified during the late Quaternary towards the margins of the central MER (Abebe et al., 2007; Agostini et al., 2011). A study of the Plio – Pleistocene and Holocene fluvio-lacustrine sequence in the central MER further indicated that late Quaternary syn-depositional tectonic activities were frequent in the region (Le Turdu et al., 1999). The Mechara area is located on the plateau adjoining the eastern margin of the MER, and have been seismically active. For instance, Ayele and Kulhánek (2000) have relocated the epicenter of the August 25, 1906 earthquake sequence (maximum magnitude of 6.5) on the eastern shoulder of the MER, just 50km south of Mechara (Asrat, 2012).

A recent probabilistic seismic hazard analysis (PSHA) for Ethiopia and the Horn of Africa region has shown that not only the rift but also the adjoining rift margins (including the Mechara area) lie within a significantly important seismic hazard zone (Ayele, 2017). The analysis considered the whole range of earthquake magnitudes recorded in the region since 1900, and calculated the Peak Ground Acceleration (PGA) corresponding to 10 % and 2 % probability of exceedance in 50 years, corresponding to return periods of 475 and 2475 years, respectively, with a spatial resolution of 0.5° x 0.5° grids. The results show PGAs ranging from 0.0 – 0.18 g and 0.0 – 0.35 g for the 475 and 2475 return periods, respectively, characterizing various parts of the Ethiopian rift and the highlands. The Mechara area lies within the zone of about 0.06 g for the 10 % and 0.13 g for 2 % probabilities, respectively. Such horizontal ground accelerations could significantly affect the aquifer architecture above the caves leading to the modification of groundwater flow paths and drip locations. The relatively short return periods of significant earthquake magnitudes closely match with the short growth phases of the Holocene stalagmites (Ach-1, Ach-3, Bero-1), and this could explain the ubiquity of discontinuous stalagmite deposition rarely lasting more than 1,000 years. Furthermore, a global synthesis of annually laminated stalagmites indicated that Ethiopian stalagmites are unique in their relatively short growth phases (with median growth duration of 172 years) compared to the median growth duration of 447 years globally (Baker et al., 2021). This feature of Ethiopian stalagmites can be attributed to the location of the Mechara caves in close proximity to an active seismic zone of the MER (see Fig. 1).

5. Conclusions

We use trace element, growth rate, $\delta^{18}O$ and $\delta^{13}C$ of Early Holocene stalagmite Ach-3 to understand the processes occurring during its deposition. The trace element composition identifies an initial growth period with a flush of soil-derived material, and a final growth period where there is a decoupling from the soil zone, indictive of drying conditions. We observe a multidecadal $\delta^{18}O$ variability in the Early Holocene Ach-3 and other two Middle and Late Holocene Ethiopian stalagmites of amplitude ~1 ‰. Covariation of $\delta^{18}O$ and $\delta^{13}C$ demonstrates that all three stalagmites are dominated by isotope fractionation, likely due to both kinetic and disequilibrium effects during the progressive degassing of CO_2 from drip waters with a high pCO_2 during stalagmite formation. The amplitude of multidecadal variability in $\delta^{18}O$ is similar to that modelled due to changes in drip rate. Rapid growth rates, fast drip rates, and isotope fractionation effects are likely the primary controls on the isotope geochemistry while active tectonics has played an important role in determining the growth duration of the three Ethiopian stalagmites, with additional influences possible from evaporative fractionation, and for samples with very short water residence time, a small primary precipitation seasonality signal. Despite the extent of non-equilibrium deposition, differences in mean stalagmite $\delta^{18}O$ through the Holocene are larger in magnitude than the multi-decadal variability. Thus long-term (centennial and longer) trends in stalagmite $\delta^{18}O$ are likely to be good proxies for climate as they record long-term climatic forcing on precipitation $d^{18}O$ and drip water $\delta^{18}O$.

Acknowledgements

Stable isotope analyses were funded by NERC National Environmental Isotope Facility grant (IP-1099-0509) and Australian Research Council LIEF funding. Fieldwork to the Mechara caves and subsequent sample preparation (lamina counting, drilling) was supported by START-PACOM, the UK Royal Society and the Leverhulme Trust. The School of Earth Sciences of the Addis Ababa University supported and facilitated fieldwork. Hilary Sloane undertook the stable isotope measurements at the National Environmental Isotope Facility. We thank John Gunn, Henry Lamb and the late Mohammed Umer, who have been very helpful during the successive field trips to the Mechara caves.

References

Abebe, B., Acocella, V., Korme, T., Ayalew, D., 2007. Quaternary faulting and volcanism in the Main Ethiopian Rift. Journal of African Earth Sciences 48, 115–124.

Agostini, A., Bonini, M., Corti, G., Sani, F., Manetti, P., 2011. Distribution of Quaternary deformation in the central Main Ethiopian Rift, East Africa. Tectonics 30, TC4010.

Asrat, A., Baker, A., Umer, M., Leng, M.J., van Calsteren, P., Smith, C.L., 2007. A high-resolution multi-proxy stalagmite record from Mechara, Southeastern Ethiopia: Palaeohydrological implications for speleothem paleoclimate reconstruction. Journal of Quaternary Science 22, 53-63.

Asrat, A., Baker, A., Leng, M.J., Gunn, J., Umer, M., 2008. Environmental monitoring in the Mechara Caves, Southeastern Ethiopia: implications for speleothem paleoclimate studies. International Journal of Speleology 37, 207-220.

Asrat, A., 2012. Speleoseismicity in the Mechara karst, Southeastern Ethiopia. In: Fairchild, I.J., and Baker, A. (2012) Speleothem Science: from Process to Past Environments. Wiley-Blackwell.

Asrat, A, Baker, A., Leng, M.J., Hellstrom, J., Mariethoz, G., Boomer, I., Yu, D., Jex, C.N., Gunn, J., 2018. Paleoclimate change in Ethiopia around the last interglacial derived from annually-resolved stalagmite evidence. Quaternary Science Reviews 202, 197-210.

Ayele, A., 2017. Probabilistic seismic hazard analysis (PSHA) for Ethiopia and the neighbouring region. Journal of African Earth Sciences 134, 257-264.

Ayele, A., Kulhánek, O., 2000. Reassessment of source parameters for the major earthquakes in the East African rift from historical seismograms and bulletins. Annali di Geofisica 43, 81-94.

Baker, A., Asrat, A., Fairchild, I.J., Leng, M.J., Wynn, P.M., Bryant, C., Genty, D., Umer, M., 2007. Analysis of the climate signal contained within $\delta^{18}O$ and growth rate parameters in two Ethiopian stalagmites. Geochimica et Cosmochimica Acta 71, 2975-2988.

Baker, A., Asrat, A., Fairchild, I.J., Leng, M.J., Thomas, L.E., Widmann, W., Jex, C., Dong, B., Calsteren, P.V., Bryant, C. 2010. Decadal scale rainfall variability in Ethiopia recorded in an annually laminated, Holocene-age stalagmite. The Holocene 20, 27-836.

Baker, A., Bradley, C., Phipps, S. J., Fischer, M., Fairchild, I. J., Fuller, L., Spotl, C., Azcurra, C., 2012. Millennial-length forward models and pseudoproxies of stalagmite$\delta^{18}O$: an example from NW Scotland. Climate of the Past 8, 1153–1167.

Baker, A., Flemons, I., Andersen, M.S., Coleborn, K., Treble, P.C., 2016. What determines the calcium concentration of speleothem-forming drip waters? Global Planetary Change 143, 152-161.

Baker, A., Hartmann, A., Duan, W., Hankin, S., Comas-Bru, L., Cuthbert, M.O., Treble, P.C., Banner, J., Genty, D., Baldini, L., Bartolomé, M., Moreno, A., and Pérez-Mejías, C. 2019. Global distribution and controls on cave drip water oxygen isotope composition. Nature Communications 10, Article number: 2984.

Baker, A., Mariethoz, G., Comas-Bru, L., Hartmann, A., Frisia, S., Borsato, A., Treble, P.C., Asrat, A., 2021. The properties of annually laminated stalagmites-A global synthesis. Reviews of Geophysics 59, e2020RG000722.

Bar-Matthews, M., Ayalon, A., Kaufman, A., 1997. Late Quaternary Paleoclimate in the Eastern Mediterranean Region from Stable Isotope Analysis of Speleothems at Soreq Cave, Israel. Quaternary Research 47, 155-168.

Bedaso, Z.K., DeLuca, N.M., Levin, N.E., Zaitchik, B.F., Waugh, D.W., Wu, S-Y., Harman, C.J., Shanko, D., 2020. Spatial and temporal variation in the isotopic composition of Ethiopian precipitation. Journal of Hydrology 585, 124364.

Borsato, A., Frisia, S., Fairchild, I. J., Somogyi, A., Susini, J., 2007. Trace element distribution in annual stalagmite laminae mapped by micrometre-resolution X-ray fluorescence: Implications for incorporation of environmentally significant species. Geochimica et Cosmochimica Acta 71, 1494–1512.

Brown, L., Gunn, J., Walker, C., Williams O., 1998. Cave Ethiopia ’95 and ’96 Expedition Report. University of Huddersfield, UK, 28p.

Bruggeman H.Y.W., 1986. Provisional Soil Association Map of Ethiopia, 1:2,000,000. Ministry of Agriculture, Addis Ababa, Ethiopia.

Corti, G., 2009. Continental rift evolution: from rift initiation to incipient break-up in the Main Ethiopian Rift, East Africa. Earth Science Reviews 96, 1-53.

Cheng, H., Edwards, R. L., Shen, C.-C., Polyak, V.J., Asmerom, Y., Woodhead, J., Hellstrom, J., Wang, Y., Kong, X., Spötl, C., Wang, X., Calvin Alexander Jr, E., 2013. Improvements in ^{230}Th dating, ^{230}Th and ^{234}U half-life values, and U-Th isotopic measurements by multi-collector inductively coupled plasma mass spectrometry. Earth. Planet. Sci. Lett. 371–372, 82-91.

Cuthbert, M.O., Rau, G.C., Andersen, M.S., Roshan, H., Rutlidge, H., Marjo, C.E., Markowska, M., Jex, C.N., Graham, P.W., Mariethoz, G., Acworth, R.I., Baker, A., 2014. Evaporative cooling of speleothems. Scientific Reports 4, Article number: 5162.

Diro, G. T., Black, E., Grimes, D. I. F., 2008. Seasonal forecasting of Ethiopian spring rains. Meteorol. Appl. 15, 73–83.

Dorale, J. A., Liu, Z., 2003. Limitations of Hendy test criteria in judging the paleoclimatic suitability of speleothems and the need for replication. Journal of Cave and Karst Studies 71 (1), 73–80.

Deininger M., Scholz D., 2019. ISOLUTION 1.0: an ISOtope evoLUTION model describing the stable oxygen ($\delta^{18}O$) and carbon ($\delta^{13}C$) isotope values of speleothems. International Journal of Speleology 48 (1), 21-32.

Dykoski, C.A., Edwards, R.L., Cheng, H., Yuan, D., Cai, Y., Zhang, M., Lin, Y. Qing, J., An, Z., Revenaugh, J., 2005. A high-resolution, absolute-dated Holocene and deglacial Asian monsoon records from Dongge cave, China. Earth and Planetary Science Letters 233, 71–86.

Edwards, R.L., Chen, J. H., Wasserburg, G. J., 1987. ^{238}U-^{234}U-^{230}Th-^{232}Th systematics and the precise measurement of time over the past 500,000 years. Earth. Planet. Sci. Lett. 81, 175-192.

Fairchild, I. J. Borsato, A., Tooth, A. F., Frisia, S., Hawkesworth, C. J., Huang, Y., McDermott, F., Spiro, B., 2000. Controls on trace element (Sr–Mg) compositions of carbonate cave waters: implications for speleothem climatic records. Chemical Geology 166, 255-269.

Fairchild, I. J., Tuckwell, G. W., Baker, A., Tooth, A. F., 2006. Modelling of dripwater hydrology and hydrogeochemistry in a weakly karstified aquifer (Bath, UK): Implications for climate change studies. Journal of Hydrology 321, 213-231.

Fantadis, J., Ehhalt, D.H., 1970. Variations of the carbon and oxygen isotopic composition in stalagmites and stalactites: Evidence of non-equilibrium isotopic fractionation. Earth. Planet. Sci. Lett. 10, 136-144.

Fleitmann, D., Burns, S.J., Mudelsee, M., Neff, U., Kramers, J., Mangini, A., Matter, A., 2003. Holocene forcing of the Indian monsoon recorded in a stalagmite from Southern Oman. Science 300, 1737–1739.

Funk, C., Hoell, A., Shukla, S., Husak, G., Michaelsen, J., 2016. The East Africa Monsoon System: seasonal climatologies and recent variations. In Carvalho L.M.V. & Jones, C. (Eds) The Monsoons and Climate Change: observations and modelling. Springer. 163–186p.

Gouin, P., 1979. Earthquake History of Ethiopia and the Horn of Africa. International Development Research Centre, Ottawa, Canada, 259p.

Gunn, J., Brown, L., 1998. Speleogenesis in the Mechara area, Western Harar, Ethiopia. Proceedings of the 2nd International Symposium on Karst Water Resources, Iran, 224-231.

Hartland, A., Fairchild, I. J., Lead, J. R., Borsato, A., Baker, A., Frisia, S., Baaloushaa, M., 2012. From soil to cave: Transport of trace metals by natural organic matter in karst drip waters. Chemical Geology 304–305, 68-82.

Hartmann, A., Baker, A., 2017. Modelling karst vadose zone hydrology and its relevance for paleoclimate reconstruction. Earth Science Reviews 172, 178-192.

Hellstrom, J. C., McCulloch, M. T., 2000. Multi-proxy constraints on the climatic significance of trace element records from a New Zealand speleothem. Earth. Planet. Sci. Lett. 179, 287-297.

Hendy, C. H., 1971. The isotopic geochemistry of speleothems — I. The calculation of the effects of different models of formation on the isotopic composition of speleothems and their applicability as palaeoclimatic indicators. Geochimica et Cosmochimica Acta 35, 801–824.

Hu, C., Henderson, G. M., Huang, J., Xie, S., Sun, Y., Johnson, K. R., 2008. Quantification of Holocene Asian monsoon rainfall from spatially separated cave records. Earth. Planet. Sci. Lett. 266, 221-232.

Le Turdu, C., Tiercelin, J.J., Gibert, E., Travi, Y., Lezzar, K., Richert, J., Massault, M., Gasse, F., Bonnefille, R., Decobert, M., Gensous, B., Jeudy, V., Tamrat, E., Mohamed, M.U., Martens, K., Balemwal, A., Chernet, T., Williamson, D., Taieb, M., 1999. The Ziway–Shala lake basin system, Main Ethiopian Rift: influence of volcanism, tectonics, and climatic forcing on basin formation and sedimentation. Palaeogeography, Palaeclimatology and Palaeoecology 150, 135–177.

Mariethoz, G., Kelly, B., Baker, A., 2012. Quantifying the value of laminated stalagmites for paleoclimate reconstructions. Geophysical Research Letters 39,L05407.

McCann, J. C., 1990. A great agrarian cycle? Productivity in highland Ethiopia, 1900 to 1987. J Interdiscip. Hist. 20(3), 389–416.

Mickler, P. J., Stern, L. A., Banner, J. L., 2006. Large kinetic isotope effects in modern speleothems. Geological Society of America Bulletin 118(1-2), 65–81.

Neff, U., Burns, S.J., Mangini, A., Fleitmann, D., Matter, A., 2001. Strong coherence between solar variability and the monsoon in Oman between 9 and 6 kyr ago. Nature 411, 290–293.

Nicholson, S.E., 2017. Climate and climatic variability of rainfall over eastern Africa. Reviews of Geophysics 55, 590-635.

Scholz, D., Mühlinghaus, C., Mangini, A., 2009. Modelling $\delta^{13}C$ and $\delta^{18}O$ in the solution layer on stalagmite surfaces. Geochimica et Cosmochimica Acta 73(9), 2592–2602.

Schulz, M., Statteger, K., 1997. SPECTRUM: spectral analysis of unevenly spaced paleoclimate timeseries. Computers and Geosciences 23, 929-945.

Segele, Z.T, Lamb, P.J., Leslie, L.M., 2009. Large-scale atmospheric circulation and global sea surface temperature associations with Horn of Africa June-September rainfall. International Journal of Climatology 29(8), 1075–1100.

Taye, M.T., Dyer, E., Charles, K.J., Hiron, L.C., 2021. Potential predictability of the Ethiopian summer rains: Understanding local variations and their implications for water management decisions. Science of the Total Environment 755, 142604.

Tooth, A. F., Fairchild, I. J., 2003. Soil and karst aquifer hydrological controls on the geochemical evolution of speleothem-forming drip waters, Crag Cave, southwest Ireland. Journal of Hydrology 273, 51-68.

Wagari Furi, 2005. Groundwater productivity and the hydrology of dry lakes basin in North-Central sector of East Harrarghe Zone. *Unpubl. MSc. Thesis*, Addis Ababa University, 89pp.

Wiedner, E., Scholz, D., Mangini, A., Polag, D., Muhlinghaus, C., Segl, M., 2008. Investigation of the stable isotope fractionation in speleothems with laboratory experiments. Quaternary International 187, 15-24.

Williams, A., Funk, C., 2011. A westward extension of the warm pool leads to a westward extension of the Walker circulation, drying eastern Africa. Climate Dynamics 37 (11–12), 2417–2435.

Viste, E., Korecha, D., Sorteberg, A., 2013. Recent drought and precipitation tendencies in Ethiopia. Theor. Appl. Climatol. 112, 535–551.

Zhang, H., Brahim, Y.A, Li, H., Zhao, J., Kathayat, G., Tian, Y., Baker, J., Wang, J., Zhang, F., Ning, Y., Edwards, R.L., Cheng H., 2019. The Asian Summer Monsoon: teleconnections and forcing mechanisms – a review from Chinese speleothem $\delta^{18}O$ records. Quaternary 2, 26.

List of Supplemental Materials

Supplemental Table 1. Trace element analysis.

Supplemental Table 2. Full spectral analysis results on both stable isotopes and growth rate time series of Ach-3 stalagmite. The dominant spectral for the respective proxy is marked in Bold.

Supplemental Figure 1. Principle Component Analysis (PCA) of trace element data.

Supplemental Figure 2. Time series of the three Principle Components (PC1 to PC3).

Supplemental Figure 3. Spectral analysis results on both stable isotopes and growth rate time series of Ach-3 stalagmite. Four spectral windows were applied (Rectangular, Welsh, Hanning and Blackman-Harris) using the SPECTRUM software (Schulz and Stattegger, 1997). The horizontal line indicates the lower bound for statistically significant power e.g. distinguished from white noise.

Supplemental Figure 4. Autocorrelation functions for $\delta^{18}O$ and $\delta^{13}C$.

Supplemental Figure 5. Spectral analysis results on oxygen isotopes for stalagmites Ach-3, Ach-1 and Bero-1. Four spectral windows were applied (Rectangular, Welsh, Hanning and Blackman-Harris) using the SPECTRUM software (Schulz and Stattegger, 1997). The horizontal line indicates the lower bound for statistically significant power e.g. distinguished from white noise. Results are tabulated in Table 2.

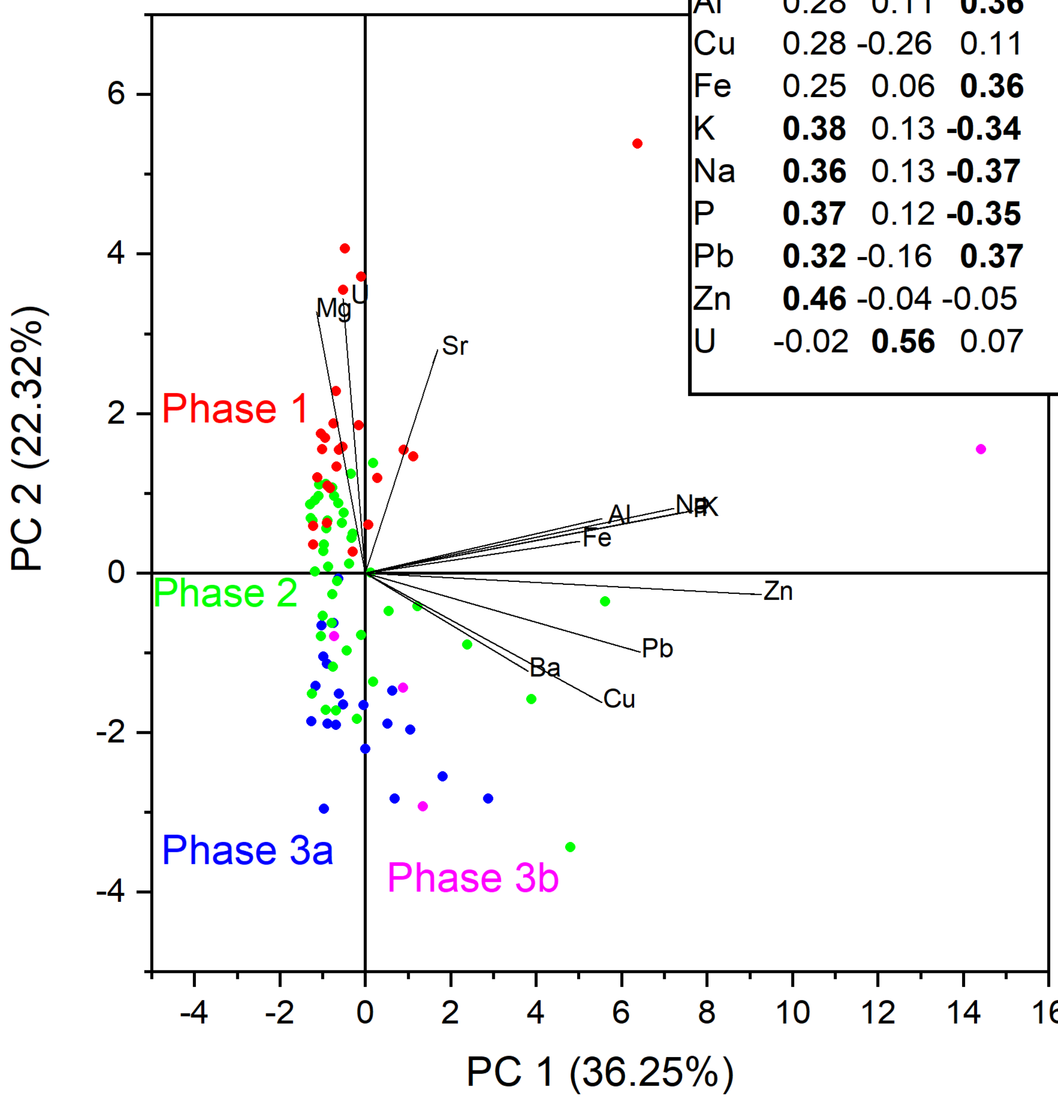

	PC1	PC2	PC3
Mg	-0.06	**0.53**	0.14
Ba	0.19	-0.20	**0.36**
Sr	0.08	**0.45**	0.24
Al	0.28	0.11	**0.36**
Cu	0.28	-0.26	0.11
Fe	0.25	0.06	**0.36**
K	**0.38**	0.13	**-0.34**
Na	**0.36**	0.13	**-0.37**
P	**0.37**	0.12	**-0.35**
Pb	**0.32**	-0.16	**0.37**
Zn	**0.46**	-0.04	-0.05
U	-0.02	**0.56**	0.07

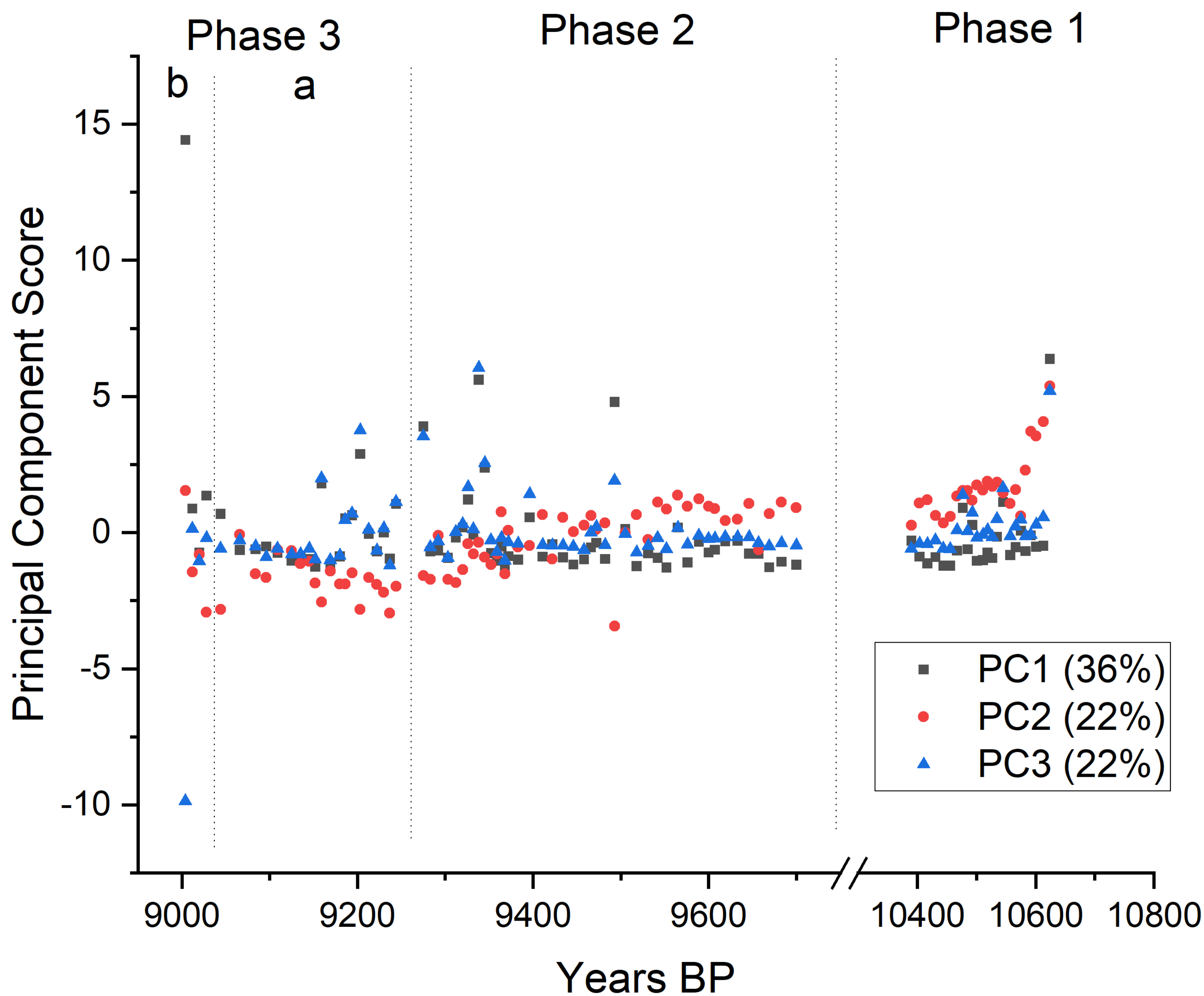
Phase 3
Phase 2
Phase 1
b
a
Principal Component Score
15
10
5
0
-5
-10
9000
9200
9400
9600
10400
10600
10800
Years BP
PC1 (36%)
PC2 (22%)
PC3 (22%)

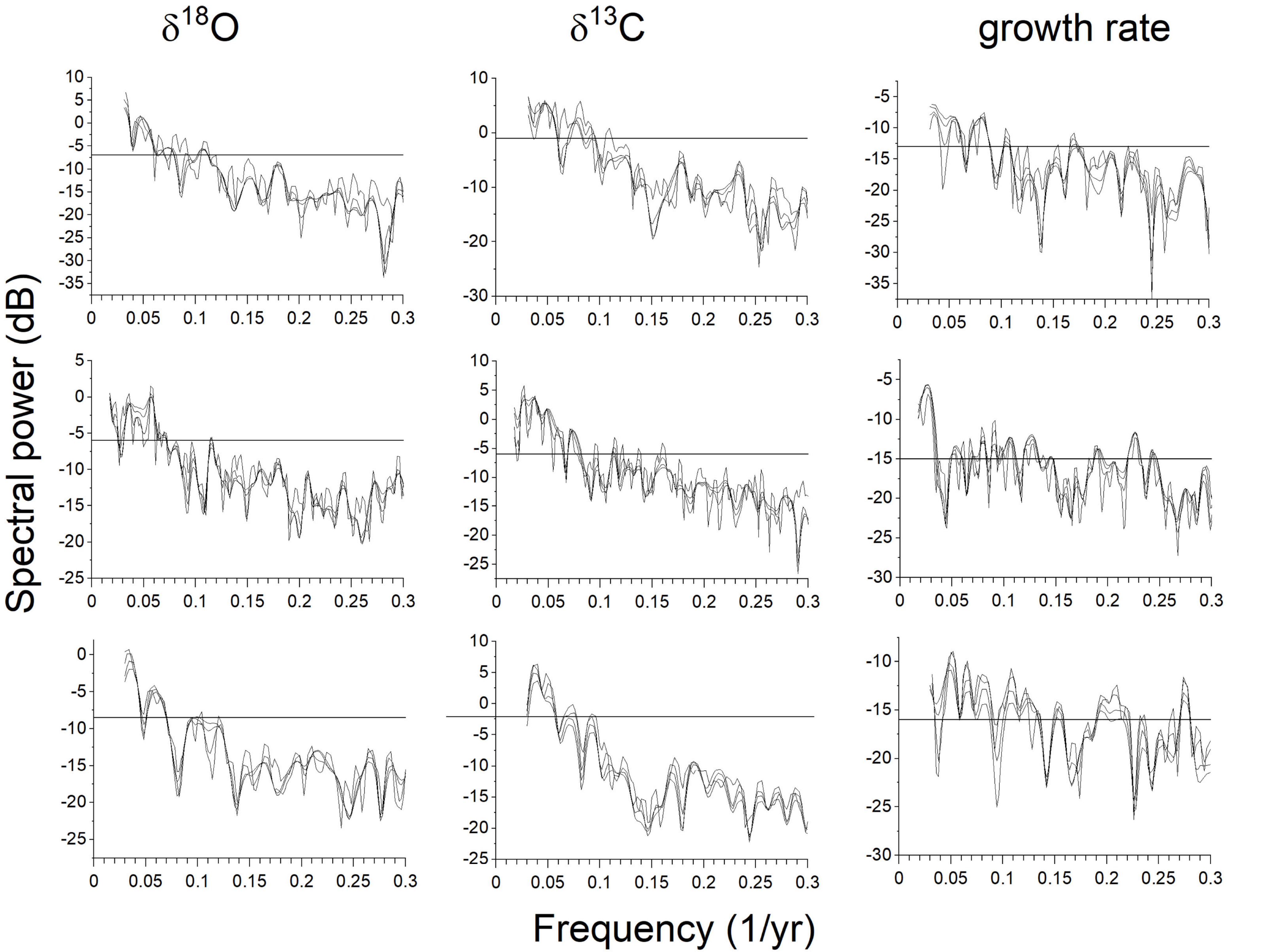

δ18O
δ13C
growth rate
Spectral power (dB)
Frequency (1/yr)

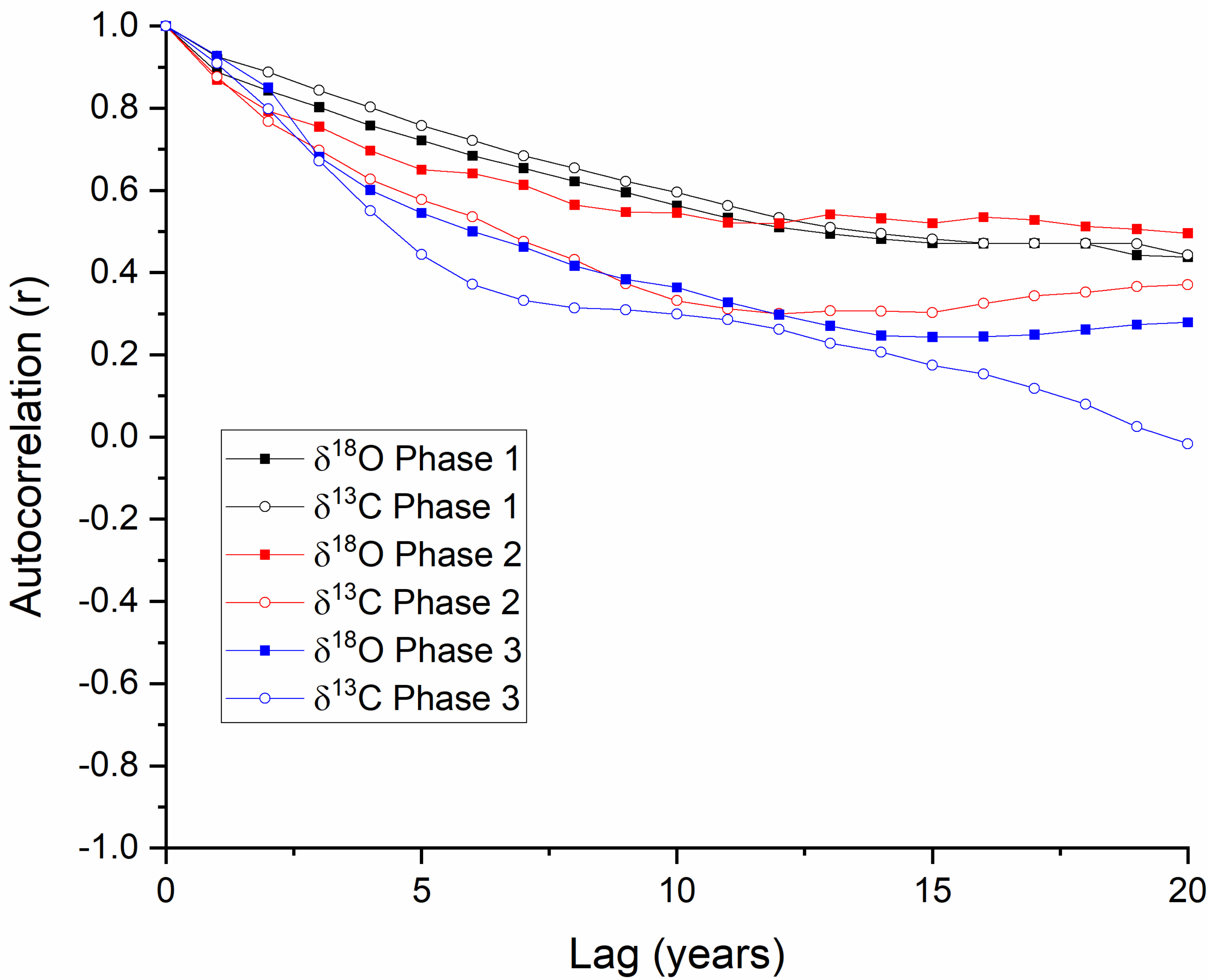
Autocorrelation (r)
1.0
0.8
0.6
0.4
0.2
0.0
-0.2
-0.4
-0.6
-0.8
-1.0
0
5
10
15
20
Lag (years)
δ18O Phase 1
δ13C Phase 1
δ18O Phase 2
δ13C Phase 2
δ18O Phase 3
δ13C Phase 3

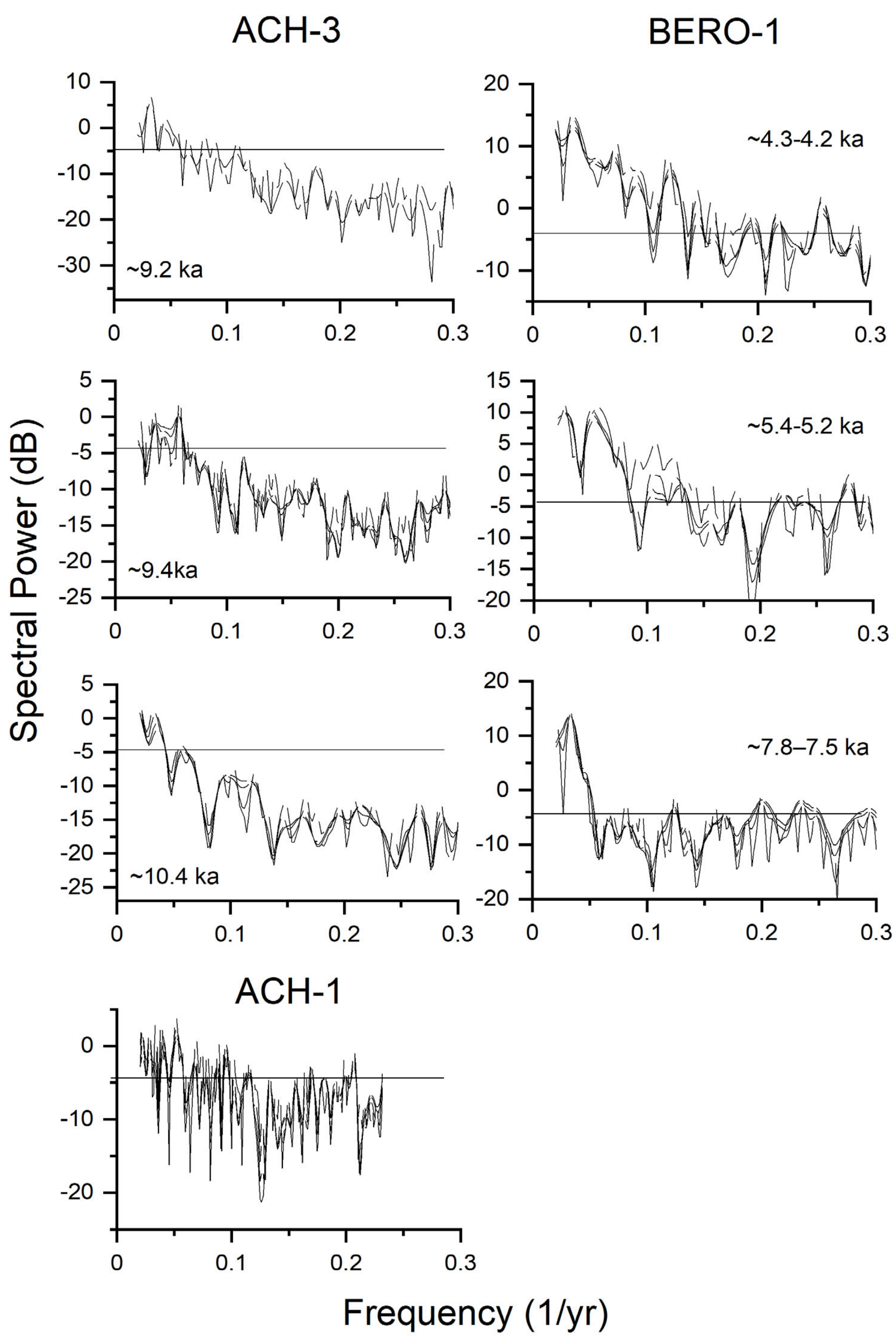

ACH-3
BERO-1
~9.2 ka
~4.3-4.2 ka
~9.4ka
~5.4-5.2 ka
~10.4 ka
~7.8–7.5 ka
ACH-1
Spectral Power (dB)
Frequency (1/yr)

Supplemental Table 1. Trace element analysis.

Sample Id	Ca	Mg	Ba	Sr	Al	Cu	Fe	K	Na	P	Pb	S	Zn	U
	wt %	wt %	mg/kg	mg/kg	mg/kg	mg/kg	mg/kg	mg/kg	mg/kg	mg/kg	mg/kg	mg/kg	mg/kg	mg/kg
ACH3-01	37.3	0.455	10.70	385	47.7	8.9	50.9	1239	759	13397	0.35	3869	23.3	1.6
ACH3-02	38.3	0.451	6.95	355	132.0	4.2	13.9	112	81	251.9	0.18	3014	3.27	1.66
ACH3-03	37.9	0.474	7.10	362	11.7	0.6	15.9	70.5	108	148.1	0.09	2966	0.88	1.79
ACH3-04	38.1	0.452	6.71	312	19.0	16.9	148.6	94	68	84.9	0.14	2526	5.42	1.67
ACH3-05	38.7	0.382	8.48	423	12.0	13.1	13.2	118	52	97	0.09	2866	4.29	1.41
ACH3-06	38.0	0.520	9.45	439	5.6	3.9	18.5	56.3	72	32.6	0.05	3305	1.40	1.75
ACH3-07	38.0	0.452	10.39	383	16.8	3.7	15.3	54.2	58.8	66.8	0.11	2964	1.21	1.61
ACH3-08	38.7	0.422	8.44	379	10.1	3.8	16.1	95	62.2	64.8	0.08	2759	1.76	1.73
ACH3-09	38.0	0.480	13.7	405	5.9	1.8	12.2	95	61.7	68.3	0.07	3200	1.03	1.75
ACH3-10	37.9	0.474	8.28	408	2.8	0.8	9.6	99	59.7	42.2	0.04	3019	0.35	1.66
ACH3-11	37.3	0.483	8.18	374	3.6	1.7	8.6	71	64.7	46.4	0.09	2723	0.91	1.56
ACH3-12	37.9	0.493	14.0	386	8.9	0.8	3.9	54.3	65.2	27.3	0.10	2567	0.61	1.58
ACH3-13	37.9	0.465	7.19	364	2.5	0.6	4.2	56.3	50.3	35.8	0.07	2437	0.28	1.40
ACH3-14	38.1	0.426	63.1	406	65.1	2.5	39.3	65.0	56.3	44.6	0.82	2436	4.67	1.48
ACH3-15	39.0	0.489	8.19	367	2.4	0.8	4.3	55.1	61.3	41.7	0.05	2774	1.08	1.64
ACH3-16	39.4	0.468	10.52	349	5.2	1.9	5.4	46.5	63.5	79.3	0.19	2703	1.18	1.71
ACH3-17	39.0	0.508	24.5	384	12.8	5.9	51.4	55.5	69	40.7	0.51	2802	3.07	1.64
ACH3-18	39.3	0.523	43.0	400	38.0	3.4	50.4	77	81	113.2	0.40	2859	2.85	1.63
ACH3-19	39.2	0.476	80.0	386	52.5	3.5	458.0	47.1	62	124.8	0.89	2429	3.85	1.42
ACH3-20	38.7	0.523	35.2	370	25.0	1.4	37.0	65.8	75	168.9	0.30	2585	1.81	1.52
ACH3-21	39.0	0.508	19.9	351	8.3	2.3	10.6	50.1	67	111.3	0.16	2521	1.51	1.56

ACH3-22	38.9	0.507	36.6	363	24.4	3.5	16.6	50.0	63	71.6	0.32	2531	2.16	1.49
ACH3-23	37.8	0.456	11.5	289	6.4	2.8	8.6	44.4	55.3	71.3	0.11	2286	1.30	1.40
ACH3-24	38.6	0.524	41.2	357	37.2	4.2	205.4	81	73	131.4	0.39	2541	2.86	1.51
ACH3-25	37.8	0.527	76.7	437	136.6	9.8	164.6	124	79	103.6	0.70	2449	7.52	1.47
ACH3-26	38.8	0.497	20.0	362	22.6	2.2	11.8	60	61	46.6	0.10	2537	1.33	1.56
ACH3-27	38.0	0.575	21.4	405	8.1	2.3	7.6	84	77	89.9	0.08	2883	1.03	1.70
ACH3-28	39.5	0.492	11.16	360	4.4	2.3	12.7	72	59.5	67.5	0.09	2556	1.11	1.65
ACH3-29	41.0	0.525	49.6	402	18.5	4.1	7.9	63	69	71.6	0.15	2663	2.00	1.69
ACH3-30	39.1	0.513	48.6	400	25.0	3.0	32.7	85	73	163.5	0.22	2744	2.31	1.67
ACH3-31	38.1	0.583	70.5	433	49.3	3.8	76.8	106	86	105.8	0.36	3070	2.90	1.66
ACH3-32	40.4	0.589	41.3	411	23.8	1.5	27.9	102	83	109.2	0.21	3144	1.88	1.72
ACH3-33	37.7	0.577	153.9	551	142.5	9.3	200.9	150	102	211.5	0.99	3045	8.24	1.62
ACH3-34	38.2	0.567	64.2	423	123.8	6.4	76.5	80	78	157.5	0.53	3070	5.44	1.61
ACH3-35	40.0	0.566	25.2	372	15.9	0.9	30.8	56.5	68	77.0	0.17	2739	0.81	1.68
ACH3-36	38.3	0.566	11.10	354	8.3	0.9	7.8	54.9	70	71.6	0.11	2813	0.94	1.67
ACH3-37	38.3	0.600	16.4	416	17.3	1.0	13.9	104	87	124.4	0.13	3457	1.31	1.92
ACH3-38	38.8	0.509	8.43	341	7.5	0.5	9.1	52.2	60	64.1	0.05	2825	0.68	1.62
ACH3-39	37.1	0.579	11.59	407	7.6	0.4	8.8	85	64	73.5	0.10	2600	0.97	1.56
ACH3-40	38.2	0.556	14.4	410	8.6	0.7	7.9	64.8	62	38.7	0.08	2646	0.59	1.53
ACH3-41	38.4	0.566	67.4	454	60.3	1.9	17.0	89	68	51.9	0.25	2671	1.95	1.55
ACH3-42	37.9	0.574	7.70	431	10.6	0.3	16.0	100	77	51.3	0.04	3128	0.70	1.76
ACH3-43	39.2	0.527	17.2	386	32.8	1.6	25.6	113	66	92.0	0.08	2818	1.64	1.65
ACH3-44	39.0	0.603	9.83	425	4.0	1.1	4.3	88	84	43.2	0.09	3319	0.71	1.89
ACH3-45	39.2	0.595	13.62	417	5.1	0.3	5.3	68	74	42.9	0.04	3200	0.08	1.71

ACH3-46	38.1	0.590	7.49	397	7.4	0.6	11.4	82.7	83	51.2	0.05	3196	0.80	1.76
ACH3-47	39.7	0.644	7.97	421	29.6	0.5	33.9	72	92	64.5	0.21	3537	1.13	1.88
ACH3-48	37.2	0.565	6.95	377	22.2	0.8	152.4	80	71	65.4	0.13	3024	0.79	1.72
ACH3-49	38.5	0.611	6.65	398	22.2	0.6	12.7	74	79	55.8	0.05	3170	0.68	1.77
ACH3-50	39.1	0.588	6.74	361	12.8	29.6	77.5	71	75	49.9	1.23	3104	15.27	1.71
ACH3-51	38.5	0.570	7.38	377	67.9	2.0	47.1	127	80	124.6	0.15	3116	2.39	1.82
ACH3-52	37.8	0.572	7.48	393	3.7	0.2	4.2	82	78	49.8	0.01	3563	0.30	1.95
ACH3-53	38.3	0.599	6.81	398	14.2	0.8	21.0	82	75	46.5	0.11	2630	1.34	1.54
ACH3-54	36.9	0.600	7.17	405	21.0	0.8	19.1	72	78	38.5	0.05	3374	0.46	1.87
ACH3-55	36.9	0.566	6.89	390	4.5	0.1	6.5	69	73	34.1	0.01	3253	0.18	1.93
ACH3-56	35.8	0.565	7.35	393	54.7	1.0	84	151	74	156.6	0.05	3367	2.46	1.88
ACH3-57	37.8	0.587	7.05	417	13.3	0.3	4.8	64.8	83	31.9	0.02	3416	0.49	1.90
ACH3-58	37.7	0.595	7.50	416	36.4	0.6	43.8	114	80	145.3	0.05	3607	2.22	1.95
ACH3-59	34.1	0.528	6.70	374	23.6	0.4	23.5	81	67	70.1	0.04	3162	1.15	1.72
ACH3-60	38.2	0.606	7.40	411	31.3	0.6	36.8	91	82	89.1	0.04	3575	1.41	1.87
ACH3-61	38.9	0.584	7.45	397	47.1	0.8	58.1	93	78	140.1	0.06	3553	2.36	1.91
ACH3-62	37.2	0.557	7.23	391	41.7	0.7	48.4	98	73	120.2	0.07	3375	2.44	1.82
ACH3-63	36.4	0.574	7.23	417	19.2	0.6	21.4	77	72	86.7	0.05	3290	1.08	1.80
ACH3-64	38.0	0.545	6.85	373	38.6	0.8	23.2	67	59	58.6	0.07	2967	1.17	1.60
ACH3-65	36.2	0.579	6.51	383	6.7	0.2	5.8	50.4	70	35.3	0.02	3168	0.46	1.75
ACH3-66	36.0	0.581	6.75	384	12.6	0.2	15.4	65.4	73	49.0	0.03	3216	0.77	1.87
ACH3-67	37.9	0.644	6.76	420	5.7	0.2	5.9	83	71	104.6	0.02	2941	0.39	1.72
ACH3-68	39.5	0.551	7.61	434	22.5	0.8	30.1	147	75	257.1	0.05	3549	2.63	1.88
ACH3-69	36.8	0.587	6.59	408	12.3	0.4	11.4	79	83	121.8	0.05	3223	0.98	1.85

ACH3-70	37.6	0.609	7.23	413	5.0	0.2	4.7	64.8	83	31.6	0.05	3648	0.55	1.94
ACH3-71	37.0	0.575	6.83	380	27.4	0.4	26.4	67.6	72	86.4	0.06	3238	0.64	1.85
ACH3-72	37.6	0.578	6.54	381	12.8	0.2	9.6	58.1	74	33.6	0.03	3325	0.36	1.82
ACH3-73	38.8	0.593	6.88	404	9.0	0.2	9.0	66	80	44.3	0.03	3478	0.30	1.94
ACH3-74	37.4	0.615	7.52	410	28.7	0.9	54.4	77	82	60.0	0.08	3587	0.61	1.95
ACH3-75	36.2	0.602	8.95	403	58.0	1.8	203.1	119	87	78.3	0.32	3586	2.18	1.92
ACH3-76	36.5	0.614	7.15	412	19.1	0.6	29.5	85	82	91.9	0.15	3647	0.88	1.92
ACH3-77	36.1	0.625	7.44	396	71.4	1.8	30.8	92	77	79.8	0.26	3322	2.49	1.77
ACH3-78	36.2	0.618	7.17	415	6.9	0.3	6.4	71	82	51.7	0.08	3584	0.33	1.93
ACH3-79	37.1	0.648	7.15	417	11.4	0.3	14.0	70	78	32.6	0.10	3537	0.45	1.88
ACH3-80	36.7	0.629	7.80	426	25.0	0.7	19.4	77	81	67.2	0.07	3699	0.84	1.96
ACH3-81	36.3	0.622	7.18	417	7.0	1.1	8.5	71	78	76.3	0.06	3564	0.82	1.92
ACH3-82	35.8	0.610	8.90	408	54.0	1.2	23.7	87	81	128.1	0.16	3735	1.47	1.95
ACH3-83	36.2	0.614	8.25	402	80.7	3.0	181.6	108	83	90.9	0.34	3655	2.61	1.89
ACH3-84	36.4	0.580	7.00	395	18.4	0.7	31.2	68	74	65.6	0.09	3563	0.76	1.89
ACH3-85	36.5	0.614	7.80	413	38.8	1.1	19.1	76	79	66.7	0.12	3763	0.96	1.92
ACH3-86	38.4	0.620	8.87	402	59.2	1.7	68.5	91	79	88.4	0.23	3649	2.09	1.85
ACH3-87	36.1	0.607	7.77	430	10.6	0.7	9.6	91	81	411.8	0.07	3882	1.00	2.08
ACH3-88	37.0	0.651	8.34	468	8.8	1.1	5.5	123	87	1525.4	0.15	3973	1.51	2.50
ACH3-89	36.6	0.695	8.00	476	9.6	0.6	8.7	91	87	596.9	0.12	3971	1.20	2.20
ACH3-90	35.7	0.698	8.00	489	6.5	0.6	7.6	88	96	388.7	0.17	4185	0.92	2.20
ACH3-91	36.3	0.674	9.40	493	240.0	3.7	577.6	241	108	2357.1	0.64	3879	9.8	2.6
MDL	**0.50**	**0.02**	**0.5**	**1.0**	**0.5**	**0.2**	**0.5**	**0.5**	**0.5**	**0.5**	**0.2**	**100.0**	**0.2**	**0.2**

Supplemental Table 2. Full spectral analysis results on both stable isotopes and growth rate time series of Ach-3 stalagmite. The dominant spectral for the respective proxy is marked in Bold.

Phase 3a (laminae 28-243)

$\delta^{18}O$

Rectangular	34-29, **25-21, 18**
Welsh I	34-29, **23-20**
Hanning	*36-29*, **23-19**
Triangular	*36-29*, **22-18**
Blackman Harris	*39-29*, **22-18**

$\delta^{13}C$

Rectangular	41-36, 25, 21
Welsh I	*41-32*, **23-21**
Hanning	*41-32*, **23-20**
Triangular	38-34, **23-20**
Blackman Harris	**23-19**

Growth Rate

Rectangular	30-26, 18, 14, 12
Welsh I	32-26, 19-18
Hanning	36-27, 19-18, 13-12
Triangular	34-26, 19-18, 13-11
Blackman Harris	34-26, 21-18, 13-12

Phase 2 (laminae 244-675)

$\delta^{18}O$

Rectangular	17.3
Welsh I	**17.3-17.6**
Hanning	**18-17**
Triangular	**18-17**
Blackman Harris	18-17

$\delta^{13}C$

Rectangular	**20-21**, 16-17, 14 yr

Welsh I	**20-21**, 14 yr
Hanning	**19-21**, 14 yr
Triangular	**20-21**, 14 yr
Blackman Harris	**20-21**, 14 yr

Growth Rate

Rectangular	39-33, 11.1
Welsh I	43-35
Hanning	43-34
Triangular	43-34
Blackman Harris	43-36

<u>Phase 1 (laminae 676-925)</u>

$\delta^{18}O$

Rectangular	*37-26*, **18-17**
Welsh I	*33-26*, **18-15**
Hanning	*33-26*, **18-15**
Triangular	*33-26*, **18-15**
Blackman Harris	*33-26*, **18-15**

$\delta^{13}C$

Rectangular	*29-25*, **21-19**, (15), (14)
Welsh I	29-25, **21-19**
Hanning	29-25, **21-19**
Triangular	29-25, **21-19**
Blackman Harris	30-26

Growth Rate

Rectangular	21-19, 15, 12
Welsh I	21-19, 15
Hanning	21-18, 13-11,
Triangular	21-19, 15, 12
Blackman Harris	21-19, 13-11